Master's thesis

NTNU
Norwegian University of Science and Technology
Faculty of Natural Sciences
Department of Physics

Siv-Marie McDougall

Fluorohectorite as a CO_2 adsorbent: a DFT and DFTB study.

Master's thesis in Applied Physics and Mathematics

Supervisor: Jon Andreas Støvneng

June 2020

NTNU
Norwegian University of
Science and Technology

Siv-Marie McDougall

Fluorohectorite as a CO_2 adsorbent: a DFT and DFTB study.

Master's thesis in Applied Physics and Mathematics
Supervisor: Jon Andreas Støvneng
June 2020

Norwegian University of Science and Technology
Faculty of Natural Sciences
Department of Physics

NTNU
Norwegian University of
Science and Technology

Abstract

In this thesis, a density functional theory (DFT) and density functional tight binding (DFTB) study is conducted to see how different cations will bind to carbon dioxide (CO_2) in fluorohectorite, in an attempt to predict whether they can be used in fluorohectorite for CO_2 storage. With DFT, the GGA revPBE exchange correlation functional is used. With DFTB, two different Hamiltonians are used; SCC-DFTB and GFN1-xTB. The cations used are Li^+, Na^+, K^+, Rb^+, Cs^+, Be^{2+}, Mg^{2+}, Ca^{2+}, Ba^{2+} and Ni^{2+}.

The results show that for both models the reaction energies seem to increase when the cation is residing in the interlayer, above the hexagonal cavity. The cation can not reside in the hexagonal cavity when the intercalated cation is too large. Also, CO_2 is likely to be parallel to the clay surface. Using the SCC-DFTB parametrization, the clay swells with increased amounts of CO_2. For one group I cation, larger cations are more tightly bound to CO_2. Using the GFN1-xTB parametrization, the reaction energy decreases when adding more CO_2 to the cations. At the same time, the cation–oxygen bond length increases. The tendency is that larger cations bind CO_2 better. Very small frequencies means a greater likelihood for a structure with CO_3 in GFN1-xTB, especially seen in the context of a short C–O distance, which especially applies to Ca-Fh and 2Cs-Fh. With increased amounts of CO_2, the C–O distance decrease, which means a weakening of the CO_2 bond.

Sammendrag

I denne oppgaven gjøres beregninger med tetthetsfunksjonalteori (DFT) og tetthetsfunksjonalteori tight binding (DFTB) på leirematerialet fluorhektoritt for å finne hvilke kationer som passer best for interkalasjon av CO_2. Med DFT blir utvekslingskorrelasjonsfunksjonalen GGA revPBE i den generaliserte gradientapproksimasjonen brukt. Med DFTB brukes to forskjellige Hamiltonier, SCC-DFTB og GFN1-xTB. Kationene som blir undersøkt er Li^+, Na^+, K^+, Rb^+, Cs^+, Be^{2+}, Mg^{2+}, Ca^{2+}, Ba^{2+} og Ni^{2+}.

Resultatene viser at reaksjonenergien øker når kationet er posisjonert over det sekskantede hulrommet og ikke inni. Dette er mulig blant annet når det interkalerte kationet er for stort til å få plass inni det sekskantede hulrommet. Dessuten ligger CO_2 oftest parallell til leireoverflaten. Med SCC-DFTB sveller leiren for økende mengder CO_2. For kationer fra gruppe I er større kationer tettere bundet til CO_2. Med GFN1-xTB minker reaksjonsenergien med økende mengder CO_2. Samtidig øker også X–O-bind-ingen. Tendensen er at større kationer binder CO_2 bedre. Veldig små strekkvibrasjoner for CO_2 i GFN1-xTB betyr en større sannsynlighet for at en CO_3-gruppe har blitt dannet, spesielt når også C–O-distansen er liten. Dette gjelder i størst grad for Ca-Fh and 2Cs-Fh. Med økende mengder CO_2 minker C–O-lengden, noe som betyr at CO_2-bindingen svekkes.

Preface

This is my Master's thesis in Applied Physics and Mathematics at the Norwegian University of Science and Technology (NTNU), and it is a continuation of my specialization project last autumn. Some of the material is reused in this thesis, including the introduction chapter, the first half of the theory chapter and parts of the method chapter.

I want to give a special thanks to my supervisor, Jon Andreas Støvneng. He has taken his time to explain physics and numerical methods every week as well as always responding to my e-mails. My questions are never too stupid to ask, which has been to great help.

I also want to thank all my friends who have taken the time to help with everything from LaTeX code, reading through my text, correcting me when I am wrong and being supportive throughout the semester. Especially thanks to Kristoffer A., Ida, Yashar, Kristoffer H., Karine, Anne, Kristoffer S. and Silius. Lastly I want to thank my family, who is only a phone call away.

My years in Trondheim have taught me a lot about physics, how to better cooperate with others and about my own shortcomings. I have learned to say no when I have to prioritize myself, that asking others for help makes stronger friendships, and that the hardest thing you do, is doing the things you do not dare to do.

Lastly, I want to thank everyone I have met throughout my studies at NTNU, through our student association Nabla, student parties and fun work in Samarbeidsforum. It has been the most social, challenging and character building years I have had so far.

Siv-Marie McDougall
Trondheim, Norway
June 2020

Contents

Abbreviations

CCS Carbon Capture and Storage

CO_2 Carbon Dioxide

DFT Density Functional Theory

DFTB Density Functional Tight Binding

GGA Generalized Gradient Approximation

LDA Local Density Approximation

NAO Natural Atomic Orbitals

PES Potential energy surface

STO Slater Type Orbitals

TS Transition State

TZP Triple Zeta Polarization

XC Exchange–Correlation

Chapter 1

Introduction

Today's political landscape is dominated by discussions about climate change and global warming. The Earth's climate does have natural variations, but the use of fossil fuels and corresponding CO_2 emissions has a massive impact on the climate [1, 2]. To keep below a 2 degree increase from pre-industrial temperature, it is crucial that the CO_2 levels in the atmosphere are lowered and that CO_2 emissions are reduced [3, 4]. This is one of the biggest challenges the world is facing, and it is therefore crucial to research ways to limit the consequences of global warming.

One possible solution is to reduce CO_2 levels by the use of carbon capture and storage (CCS). It is therefore essential to know more about how CO_2 works in the atmosphere, how far the technology behind CCS has come, and how Fluorohectorite can be a part of the solution.

1.1 Carbon Dioxide in the Atmosphere

Energy from the Sun radiates to Earth, and around 70 % of this energy is absorbed by the Earth's ground and atmosphere. When electromagnetic waves of energy arrive to Earth from the Sun in various frequencies, circa one third of it is reflected back into space by clouds, the atmosphere and the Earth. The rest of it is absorbed to the ground and in the atmosphere. To achieve a stable temperature on Earth, the flow of incoming solar energy and outgoing radiation must be at equilibrium: $\text{Energy}_{\text{in}} = \text{Energy}_{\text{out}}$. In the lower atmosphere, energy in the infrared spectrum is trapped by CO_2, causing the energy to remain in the atmosphere instead of escaping out into space. This keeps the temperatures on Earth above a livable temperature range. Trapping heat in-

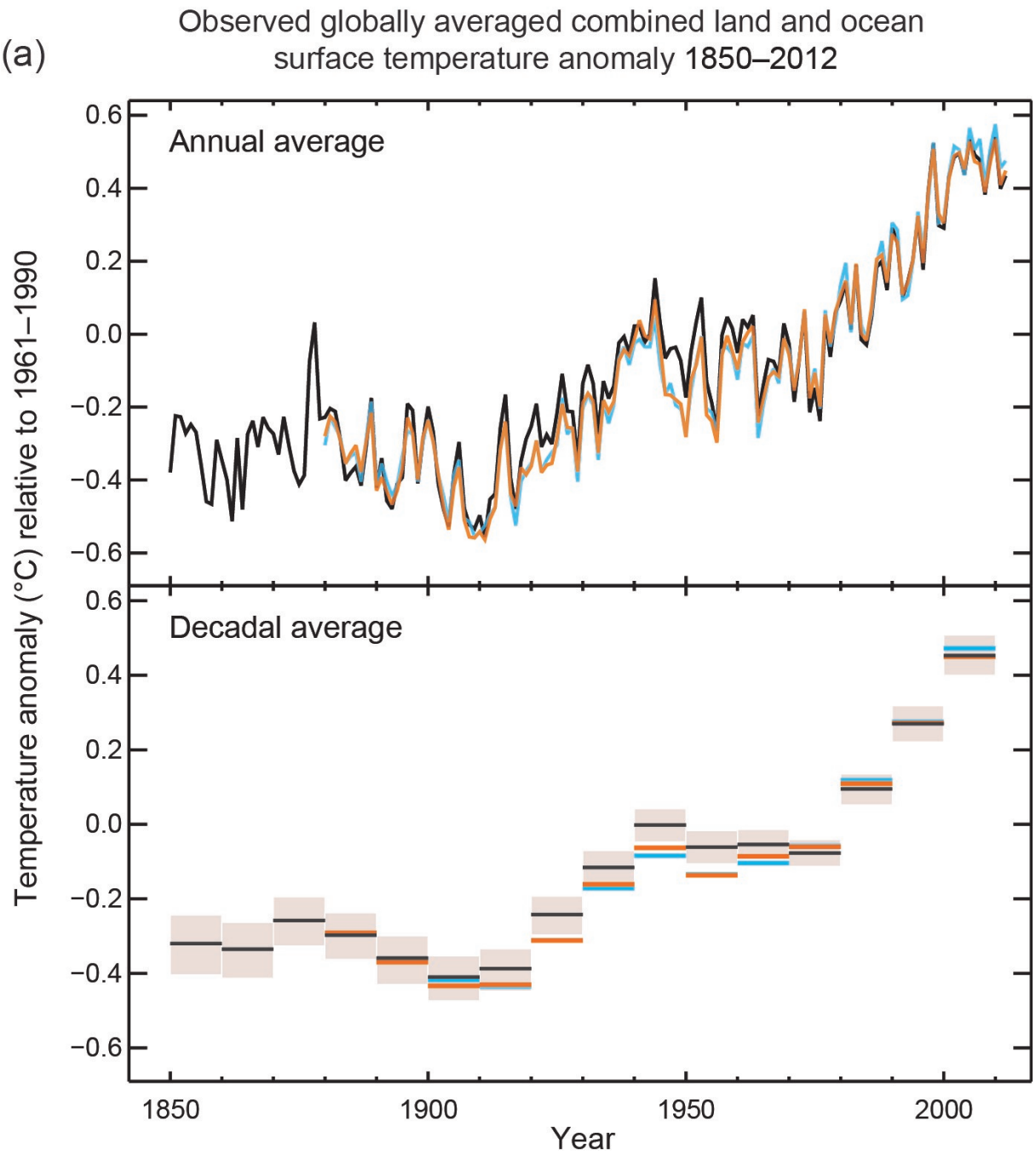

Figure 1.1: The development of atmospheric temperature, taken from [2, Figure SPM.1 (a)].

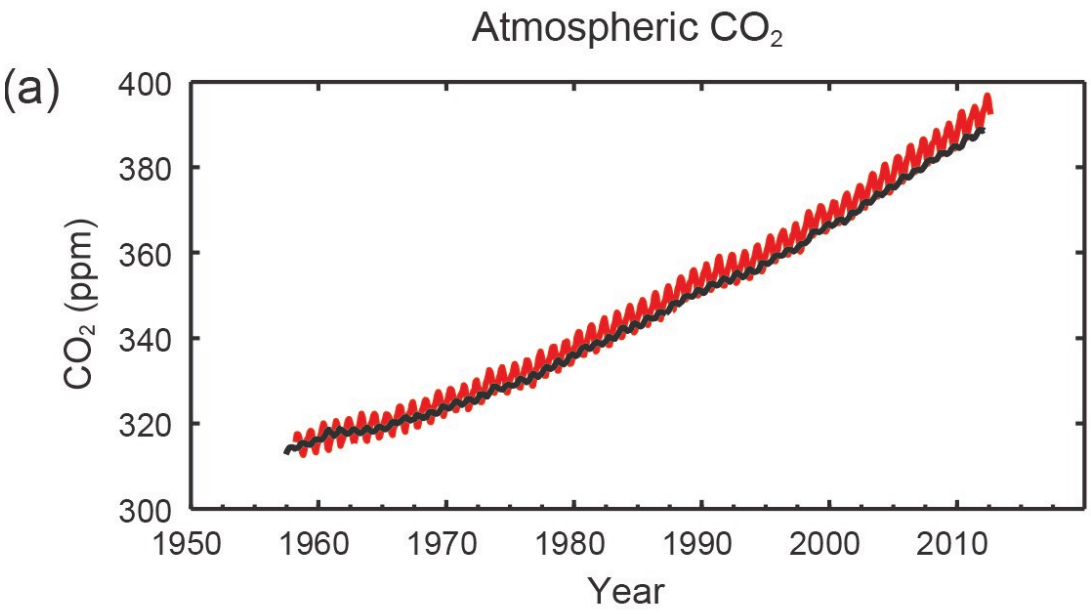

Figure 1.2: The development of atmospheric CO_2 concentrations, taken from [2, Figure SPM.4 (a)].

side a closed space is also the concept of a greenhouse, and it is why gases in the atmosphere, such as CO_2, are referred to as greenhouse gases [5, Chapter 2].

An increasing amount of CO_2 in the atmosphere causes the temperature on Earth to rise [5, Chapter 2]. Figure 1.1 shows the development of the atmospheric temperature over the last 150 years, and Figure 1.2 shows the CO_2 concentrations over the last 50 years. With increasing amounts of CO_2, the atmosphere traps increasing amounts of energy instead of letting excess heat radiate out into space, which leads to increasing temperatures on Earth. Other greenhouse gases like methane and chlorofluorocarbon (CFC) gases will also cause this behaviour. However, the amount of these is not in the same scale as CO_2. CO_2 is the greenhouse gas with the largest concentration in the atmosphere, and it is also the greenhouse gas which humans emit at the highest rate. Research shows that there is a correlation between the increase in CO_2 concentrations in the atmosphere and the increase in the temperature on Earth [1, 2].

1.2 Carbon Capture and Storage

Carbon capture can be done either from a point-source or directly from the atmosphere [6]. The most energy efficient and easiest way to capture CO_2

is from inserted filters in power plants and factories, called point-sources. This only reduces the local CO_2 emissions. To prevent CO_2 emission from airplanes and cars, one would have to capture CO_2 from the atmosphere. The latter technology has been around for years in small scale, for example to extract CO_2 from the air in submarines [6]. The amount of CO_2 in air is 1:2500, which means one would have to process large volumes of air with an energy-intensive extraction process in order to extract large amounts of CO_2 from the atmosphere. Modifying the air by cooling or pressurizing it would require too much energy [6]. A better solution is to collect air through large fans and absorb or adsorb CO_2 in various ways, for example like Climework does [7, 8]. The energy to drive the CO_2 capture processes has to be restricted to limit the CO_2 emissions from the process and hence capture more CO_2 than is emitted. One way to restrict the energy usage is to use nearby green energy sources like wind and thermal power, or low-grade waste heat.

After capturing CO_2, it needs to be stored, and there are several possible storage methods. All methods used today look at how CO_2 will adsorb to the surface or interface of a material, or be absorbed into the material [6]. Adsorption is when an atom bonds with the surface atoms of a material [9, p. 103]. One method is to send the gas mixed with water underground and letting it react with basaltic rocks to form stone [10, 5]. An important aspect of storing CO_2 is that it has to be cheap for the technology to be competitive. Another crucial aspect is that storage sites should not leak CO_2 over time [6]. Leakage means a less efficient system and one would have to capture more CO_2 to make up for the leaked CO_2. A material that seems to fulfill these requirements is clay, which has potential as a future carbon storage material and is the focus of this thesis.

1.3 Clay and Fluorohectorite

Today researchers are looking into storing carbon in clay. Clay is abundant, cheap, reusable and non-toxic [11]. The surface area of clay is large which gives clay a good adsorption capacity. It is therefore worth looking closer at the properties of clay, and especially fluorohectorite, which is the specific type of clay used in this thesis.

Clay is a mineral with grain size smaller than 2 µm and is found in large parts on Earth. It makes up around 10 % of the volume of the Earth's crust and is a mineral with a layered structure called phyllosilicates [5, pp. 56–58]. The def-

inition of a mineral is: "A naturally occurring solid inorganic (usually) substance with a definite chemical formula and an ordered atomic structure" [5, p. 56]. Clay also has a specific atomic formula, unlike for example stone, which often is a collection of different atomic formulas. Many clay minerals need water to form as part of the structure [5, p. 34].

The stacking arrangement of the clay sheets is the main property to define a clay mineral. On an atomic level, clay can be tetrahedral or octahedral, depending on the placing of the cations of the unit cell. Clay can be categorized in two main stacking arrangements: a 1:1 and a 2:1 layer, which is a ratio between the tetrahedral and octahedral sheets. The 1:1 type is put together by a tetrahedral and an octahedral sheet. The 2:1 type consists of two tetrahedral and one octahedral sheet per layer. Both stacking arrangements are illustrated in Figure 1.3. A variation of the 2:1 type is one where there are two tetrahedral and one octahedral sheet per layer and an octahedral sheet associated with the layer, this is often referred to as 2:2. The different types of layers affect the structure of the clay and the properties of the mineral, such as surface charge and the ability to swell [5, p. 61].

Interchanging one of the cations in the octahedral sheet of clay, with a cation of different valence, will give the sheet a different charge. The most normal is to interchange a cation with a lower valence cation, for example interchange Al^{3+} with Mg^{2+} in montmorillonite, or Mg^{2+} with Li^{+} in hectorite. This gives a net negative charge of the sheet. Thus an extra cation needs to be added to the unit cell to make the sheet neutral. The cation can be added to the interlayer or within the layers [5, p. 60]. The cation added in the interlayer will be mobile and can be interchanged with other cations.

Hectorite, and thus also fluorohectorite, is a smectite clay material. It is monoclinic, which means it has a crystal structure with two right angles and one angle that is different from 90°. It has a 2:1 type layer. In this thesis, the hectorite chosen for computations was fluorohectorite, as it has been of experimental interest at the Department of Physics at NTNU [12]. Fluorohectorite has the formula

$$X_y(Mg_{6-y}Li_y)Si_8O_{20}F_4. \tag{1.1}$$

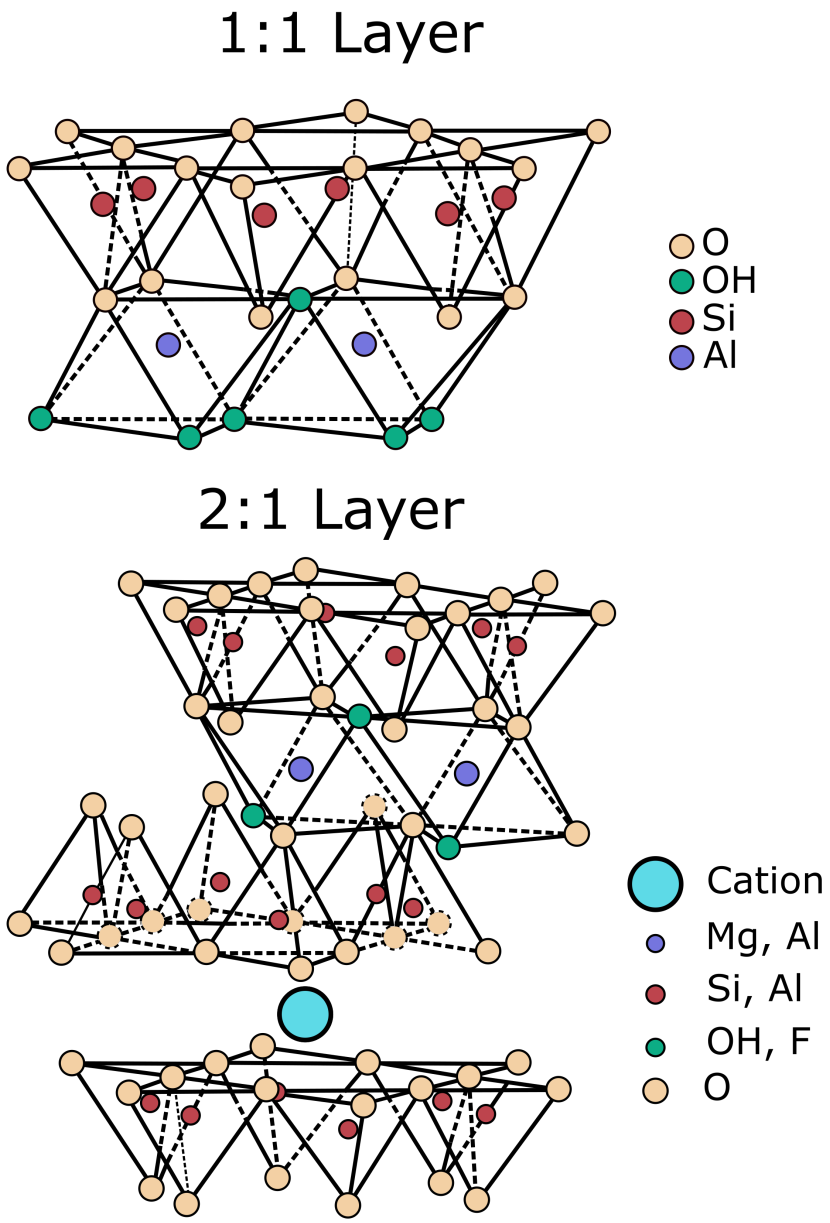

Figure 1.3: Illustration of the 1:1 and 2:1 layer geometry of clay, used with permission from [12, Figure 2.2].

This means that every unit cell has 38 atoms in total when $y = 0$, where 20 of these are O, 8 are Si and 4 of them are F. In the octahedral layer there are then 6 atoms of Mg. If $y \neq 0$, the octahedral layer will have $6 - y$ Mg atoms and y Li atoms. With 6 Mg atoms in the octahedral layer, the unit cell is neutral. Mg has a chemical valence of two, while Li has a chemical valence of one. This means that when interchanging a Mg atom for a Li atom, the total unit cell has a negative net charge. Therefore, a metal ion with positive charge must

be found in the interlayer to neutralize the charge. The geometry of (1.1), with X = Na and $y = 1$, is illustrated in Figure 1.4.

Fluorohectorite will be shortened to Fh for simplicity. Fh with one cation as the interlayer cation, which means $y = 1$ in equation 1.1, gives X-Fh. For sodium as the interlayer cation, this would be shortened as Na-Fh. This also holds for divalent cations. With two cations in the interlayer, for example with sodium again, X = Na and $y = 2$, it will be 2Na-Fh for short.

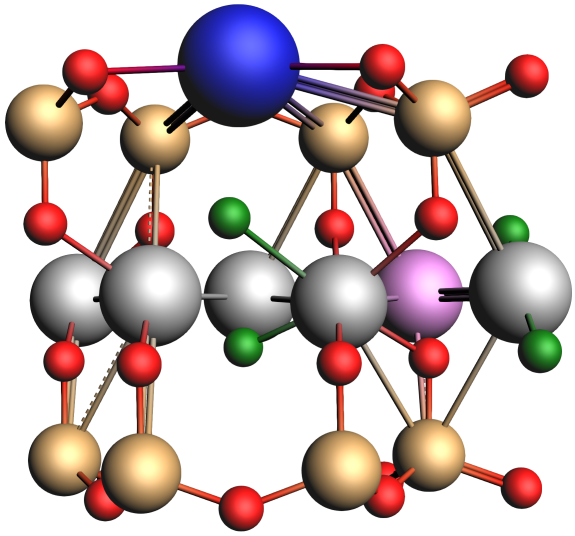

Figure 1.4: The unit cell geometry of $Na(Mg_5Li)Si_8O_{20}F_4$ pictured in the xz-plane. Color code: Mg = gray; Li = magenta; F = green; O = red; Si = gold; Na = blue. Figure made in Amsterdam Modelling Suite.

CO_2 can adsorb to the clay mineral by bonding with the atoms in the interlayer [5, p. 107]. Because of the layered structure of clay, the atoms of CO_2 will in this case bond with the interlayer. When clay adsorbs a molecule like CO_2 into the interlayer, it often results in the volume of clay expanding, referred to as swelling [5, p. 107].

1.4 Structure of the Report

In this thesis, DFT and DFTB calculations were done to see how well different interlayer cations in fluorohectorite adsorb CO_2, looking at cations in group I and II as well as nickel. The following chapter will go through the theory behind DFT and DFTB. Chapter 3 gives an overview of the computational details, followed by Chapter 4 where the results will be presented along with

discussions of the results. Lastly, Chapter 5 will give some concluding remarks and thoughts on further work on the topic.

Chapter 2

Density Functional Theory

The main aim with DFT calculations on a many body problem is to find the most stable molecule structure. The most stable structure for a molecule is the structure that has the lowest ground state energy, E_0. To find the answer to this, the Schrödinger equation has to be solved.

The background for DFT was laid in 1964 and in 1965 by Kohn and Hohenberg [13], and Kohn and Sham, respectively [14]. It has since become a well-known and well-used method to solve calculations in computational physics and chemistry, especially after its breakthrough in 1990 when the accuracy of the method was refined [15]. In 1998, Walter Kohn won the Nobel Prize in chemistry for the foundation of DFT, shared with John Pople for his quantum chemistry computer methods [16].

2.1 Schrödinger's Equation in a Many Body Problem

Looking at a molecule means looking at multiple nuclei at the same time, which means working with a many body problem. Solving the Schrödinger equation for a many body problem is more complicated than for just a one body problem, with a more complicated Hamiltonian.

This problem can be split in two mathematical problems because of the fact that the nuclei are much heavier than the electrons. This is known as the *Born–Oppenheimer approximation*. First the nuclei can be seen as fixed in space, while the problem is solved for the motion of the electrons. With M nuclei at positions $\mathbf{R}_1$,...,$\mathbf{R}_M$, the ground state energy of the system will depend on the positions, $E(\mathbf{R}_1,...,\mathbf{R}_M)$. When this is calculated, it is possible to solve the Schrödinger equation for nuclei that are moved around. The

Schrödinger equation can be written as

$$\hat{H}\psi = \left[-\frac{\hbar^2}{2m} \sum_{i=1}^{N} \nabla_i^2 + \sum_{i=1}^{N} V(\mathbf{r}_i) + \sum_{i=1}^{N} \sum_{j<i} U(\mathbf{r}_i, \mathbf{r}_j) \right] \psi = E\psi, \tag{2.1}$$

where $\hat{H}$ is the Hamiltonian, ψ is the electron wave function, m is the electron mass and E is the ground state energy . Here the electronic spin is neglected. Inside the brackets, the three terms are kinetic energy for the electrons, the potential energy between a single electron and nuclei as a collection, and the energy due to the electron–electron interaction [9, p. 10]. ψ is a function of the coordinates of all the N electrons, thus $\psi = \psi(\mathbf{r}_1, ..., \mathbf{r}_N)$. However, for a many body problem, this can be approximated by multiplying the different wave functions for the individual N electrons, $\psi = \psi_1(\mathbf{r}_1)\psi_2(\mathbf{r}_2)...\psi_N(\mathbf{r}_N)$, assuming all particles are independent.

2.2 Reciprocal Space and Bloch's Theorem

A crystal in real space with lattice vectors $\mathbf{a}_1$, $\mathbf{a}_2$ and $\mathbf{a}_3$ can be expressed in terms of atomic coordinates $\mathbf{R} = n_1\mathbf{a}_1 + n_2\mathbf{a}_2 + n_3\mathbf{a}_3$, where n_i are arbitrary integers [9, p. 51].

The properties of crystalline materials can be computed accurately with DFT calculations. Crystals are conveniently described in reciprocal space due to their periodic nature, and it is therefore relevant to look at the concepts of reciprocal space, often referred to as momentum space or $\mathbf{k}$-space, where $\mathbf{k}$ is the wave vector. $\mathbf{k}$ in reciprocal space is equivalent to $\mathbf{r}$ in real space. The reciprocal lattice is the representation of the Fourier transform of the crystal lattice structure. With the plane wave $e^{i\mathbf{k}\cdot\mathbf{r}}$, the definition of the reciprocal lattice is that $\mathbf{k}$ has to satisfy $e^{i\mathbf{k}\cdot\mathbf{R}} = 1$ for all $\mathbf{R}$ [17, p. 12]. The reciprocal lattice vectors are $\mathbf{b}_1$, $\mathbf{b}_2$ and $\mathbf{b}_3$. By definition, $\mathbf{a}_i \cdot \mathbf{b}_j = 2\pi\delta_{ij}$, where $\delta_{ij} = 1$ when $i = j$ and 0 otherwise. This gives the following relation between the real space lattice vectors and the reciprocal lattice vectors:

$$\mathbf{b}_1 = 2\pi \frac{\mathbf{a}_2 \times \mathbf{a}_3}{\mathbf{a}_1 \cdot (\mathbf{a}_2 \times \mathbf{a}_3)}, \quad \mathbf{b}_2 = 2\pi \frac{\mathbf{a}_3 \times \mathbf{a}_1}{\mathbf{a}_2 \cdot (\mathbf{a}_3 \times \mathbf{a}_1)}, \quad \mathbf{b}_3 = 2\pi \frac{\mathbf{a}_1 \times \mathbf{a}_2}{\mathbf{a}_3 \cdot (\mathbf{a}_1 \times \mathbf{a}_2)}. \tag{2.2}$$

The reciprocal lattice vectors define the unit cell in the reciprocal space, which is called the first Brillouin zone. The Brillouin zone is important in the band

theory of materials. From the definition it is can be seen that the volume of the Brillouin zone, V_{BZ}, and the volume of the cell in real space, V_{cell}, have the relation

$$\mathrm{V_{BZ}} = \frac{(2\pi)^3}{\mathrm{V_{cell}}}. \tag{2.3}$$

This means that a large volume in real space gives a small volume in reciprocal space and vice versa.

The wave functions for the electrons moving in a non vanishing periodic potential in crystals must satisfy Bloch's theorem which states

$$\psi_k(\mathbf{r}) = e^{i\mathbf{k}\cdot\mathbf{r}} u_k(\mathbf{r}). \tag{2.4}$$

Here $u_k(\mathbf{r})$ is a lattice periodic function with the same periodicity as the lattice, namely $u_k(\mathbf{r}+\mathbf{R}) = u_k(\mathbf{r})$. Because of this periodicity, the first Brillouin zone explains the physics of the material. These *Bloch waves* are illustrated in Figure 2.1.

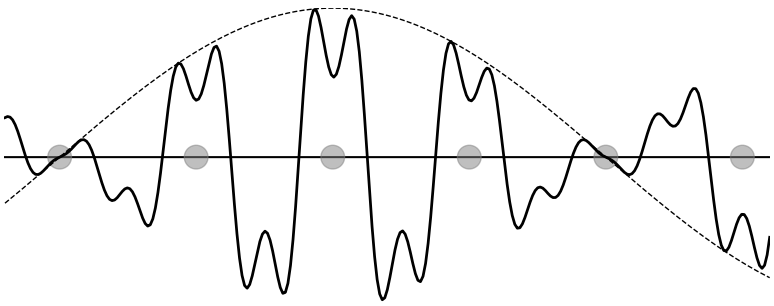

Figure 2.1: The real part of the Bloch wave in one dimension. The grey circles denote atoms. The dotted line is from the plane wave, $e^{i\mathbf{k}\cdot\mathbf{r}}$.

2.3 The Hartree–Fock Method

The Hartree–Fock method is an iterative method that approximates the energy and wave function of a many body problem. Equation (2.1) can be simplified by assuming that there is no electron–electron interaction between the N electrons. In this case, the Hamiltonian can be written

$$H = \sum_{i=1}^{N} h_i, \tag{2.5}$$

where h_i takes into account the kinetic and potential energy for electron i. This gives the Schrödinger equation for one electron: $h\chi = E\chi$. The spin of

each electron is included by constructing spin orbital eigenfunctions that can be written as $\chi_j(\mathbf{x}_i)$ ($j = 1, 2...$), where $\mathbf{x}_i$ expresses the position and spin state of electron i [9, p. 20]. The energy for spin orbital χ_j is denoted E_j. The simplest total wave function for a system of N electrons is called the Hartree product. It is the product of the wave functions for the single electron spin orbitals, χ_j:

$$\psi(\mathbf{x}_1, ..., \mathbf{x}_N) = \chi_{j_1}(\mathbf{x}_1)\chi_{j_2}(\mathbf{x}_2)...\chi_{j_N}(\mathbf{x}_N). \tag{2.6}$$

Summing the energies of the spin orbitals gives the total energy of the system. Electrons are fermions, hence the wave function must change sign if two electrons are interchanged due to the antisymmetry principle [18]. This is not a feature the Hartree product possesses. That is why the Slater determinant for N electrons is more appropriate,

$$\psi(\mathbf{x}_1, ..., \mathbf{x}_N) = \frac{1}{\sqrt{N!}} \begin{vmatrix} \chi_1(\mathbf{x}_1) & \chi_2(\mathbf{x}_1) & ... & \chi_N(\mathbf{x}_1) \\ \chi_1(\mathbf{x}_2) & \chi_2(\mathbf{x}_2) & ... & \chi_N(\mathbf{x}_2) \\ ... & ... & ... & ... \\ \chi_1(\mathbf{x}_N) & \chi_2(\mathbf{x}_N) & ... & \chi_N(\mathbf{x}_N) \end{vmatrix}. \tag{2.7}$$

The factor in front of the determinant is a normalizing factor. The sign of the Slater determinant will change if two electrons are interchanged, mathematically represented by changing the determinant's rows. This is therefore a good way to represent a system of fermions. If two electrons are in the same state, the Slater determinant will become zero, as it should to fulfill the Pauli principle. As an example for two electrons, the Slater determinant becomes

$$\psi(\mathbf{x}_1, \mathbf{x}_2) = \frac{1}{\sqrt{2}} \left[\chi_j(\mathbf{x}_1)\chi_k(\mathbf{x}_2) - \chi_j(\mathbf{x}_2)\chi_k(\mathbf{x}_1) \right], \tag{2.8}$$

which is zero when $\chi_j = \chi_k$ [9, p. 20]. The Pauli principle says that two identical fermions cannot occupy the same quantum state at the same time, that is, the same orbital state and spin. This means $\psi(\mathbf{x}_1, \mathbf{x}_2)$ satisfies the Pauli principle. Hartree–Fock calculations are similar to DFT. By fixing the atomic nuclei in space and then look at the N electron wave function, the Schrödinger equation becomes

$$\left[-\frac{\hbar^2}{2m}\nabla_j^2 + V(\mathbf{r}) + V_H(\mathbf{r}) \right] \chi_j(\mathbf{x}) = E_j \chi_j(\mathbf{x}). \tag{2.9}$$

In the brackets, the first two terms are as in Equation (2.1), while the third term is the Hartree potential

$$V_H(\mathbf{r}) = e^2 \int \frac{n(\mathbf{r}')}{|\mathbf{r} - \mathbf{r}'|} d^3 r'. \tag{2.10}$$

This means that an electron feels the average Coulomb potential from the other electrons. The spin orbitals can be approximated as

$$\chi_j(\mathbf{x}) = \sum_{i=1}^{K} \alpha_{j,i} \phi_i(\mathbf{x}). \tag{2.11}$$

The expansion coefficient is expressed by $\alpha_{j,i}$. The basis set, ϕ, is a finite set of functions from ϕ_1 to ϕ_K. From this it is obvious that the calculations will be more precise with a larger K, thus a larger basis set [9, p. 22]. However it will also require more computing capacity.

This is everything needed to do the Hartree–Fock calculations. The next step is to make a guess for the spin orbitals by specifying $\alpha_{j,i}$. Then, the electron density, $n(\mathbf{r})$, must be calculated to find the single electron spin orbitals. The electron density at a position in space depends on the individual electron wave functions:

$$n(\mathbf{r}) = 2 \sum_i \psi_i^*(\mathbf{r}) \psi_i(\mathbf{r}), \tag{2.12}$$

where the factor of 2 reflects the two spin states of electrons. This procedure has to be repeated until the calculated spin orbitals are close enough to the initial guess, hence the calculations have to reach a pre-chosen convergence limit before the calculations have converged.

The Hartree–Fock calculations do not take into consideration all the electron–electron interactions. This means that the energy found with the Hartree–Fock method will not be the true energy of the system. The difference between the exact energy and the Hartree–Fock energy is usually called the correlation energy.

2.4 The Kohn–Sham Equations

An alternative to the Hartree–Fock method is DFT. The first fundamental theorem for DFT is: "The ground-state energy from Schrödinger's equation is a unique functional of the electron density" [9, p. 11], formulated by Kohn and Hohenberg. This means that there is a one-to-one mapping between the wave function and the electron density. A functional takes a function and defines a single number from it. An example of a functional is

$$F[f] = \int_{-1}^{1} f(x)\,dx, \tag{2.13}$$

where $f(x)$ is the function and $F[f]$ is its functional. By using, e.g., $f(x) = x^3 - 1$, one gets $F[f] = -2$. This then means that the energy can be expressed by the electron density, $E[n(\mathbf{r})]$. By using a functional, the $3N$ variable problem for finding the ground state energy is reduced to finding the electron density, a function of 3 spatial variables.

However, the theorem does not specify what the functional actually is. That is why the second theorem is helpful: "The electron density that minimizes the energy of the overall functional is the true electron density corresponding to the full solution of the Schrödinger equation" [9, p. 12]. This can also be expressed with the energy functional for the single electron wave function, ψ_i:

$$E[\psi_i] = E_{\text{known}}[\psi_i] + E_{\text{XC}}[\psi_i], \tag{2.14}$$

where E_{known} is all the energy terms already known, and E_{XC} is all other energies, like the many body terms. E_{XC} is also known as the exchange–correlation (XC) functional. The known terms for the energies are the electron kinetic energy, the electron–nuclei Coulomb interaction, the electron–electron Coulomb interaction, and the Coulomb interactions between nuclei:

$$\begin{aligned} E_{\text{known}}[\psi_i] = -\frac{\hbar^2}{2m}\sum_{i=1}\int \psi_i^* \nabla^2 \psi_i\, d^3r + \int V(\mathbf{r})\, n(\mathbf{r})\, d^3r \\ + \frac{e^2}{2}\int\int \frac{n(\mathbf{r})\, n(\mathbf{r}')}{|\mathbf{r}-\mathbf{r}'|} d^3r\, d^3r' + E_{\text{ion}}. \end{aligned} \tag{2.15}$$

The final Kohn–Sham equations are

$$\left[-\frac{\hbar^2}{2m}\nabla_i^2 + V(\mathbf{r}) + V_H(\mathbf{r}) + V_{\mathrm{XC}}(\mathbf{r})\right]\psi_i(\mathbf{r}) = \varepsilon_i\psi_i(\mathbf{r}), \tag{2.16}$$

which is similar to Equation (2.1). This equation is only based on 3 variables and the single-electron wave function and hence no sum as in the Schrödinger equation (2.1). The three potential terms on the left-hand side are, respectively, the potential for interaction between the electron and the collection of nuclei, the Hartree potential and the potential for the exchange–correlation functional:

$$V_{\mathrm{XC}}(\mathbf{r}) = \frac{\delta E_{\mathrm{XC}}(\mathbf{r})}{\delta n(\mathbf{r})}. \tag{2.17}$$

This is formally the functional derivative of the exchange–correlation energy.

2.5 The Exchange–Correlation Functional

Kohn–Sham's theorems do not give the solution for the exact functional, it merely states that it exists and the definition of it. To solve DFT problems with many atoms, we want to find a functional that explains the world as precisely as possible and can be solved mathematically. This is yet to be done, but instead it is possible to make a functional that is simpler and somewhat similar to the true functional.

The simplest form for the exchange–correlation functional is the local density approximation (LDA), when assuming the material in question is a uniform electron gas and that $n(\mathbf{r})$ is constant:

$$V_{\mathrm{XC}}^{\mathrm{LDA}}(\mathbf{r}) = V_{\mathrm{XC}}^{\text{uniform electron gas}}[n(\mathbf{r})]. \tag{2.18}$$

Of course, this is not a perfect representation of real materials, where the density varies, and hence, it is not the true exchange–correlation functional for a material.

Another class of functionals that has been shown to work well, is the generalized gradient approximation (GGA). As well as having information about the local electron density, it also has information about the local gradient in the electron density, more specific the derivative of the electron density:

$$V_{\mathrm{XC}}^{\mathrm{GGA}}(\mathbf{r}) = V_{\mathrm{XC}}[n(\mathbf{r}), \nabla n(\mathbf{r})]. \tag{2.19}$$

This has more physical information than LDA, which makes it less an approximation and closer to the exact solution. However, it will also require more computing, and it will not always be a better functional simply because it includes more information. Incorporating more information to the problem means the probability increases for systematic errors in DFT calculations versus what true nature looks like.

There are several different GGA functionals, and one of the most used ones is the Perdew–Burke–Ernzerhof (PBE) functional. This is a non empirical functional which satisfies the uniform density limit. The revised PBE, namely revised GGA PBE (GGA revPBE), is also a much used funtional and is more accurate than the PBE, especially when it comes to atoms and molecules bonding to surfaces [19]. revPBE also improves the total atomic energies and reduces the maximum absolute error compared to PBE [20].

2.6 Potential Energy Surfaces and Normal Modes

The potential energy of a molecule depends on the coordinates of the individual atoms in the molecule. This is referred to as the potential energy surface (PES). Hence, if the atoms in the molecule move, the potential energy changes [21, p. 4]. With a system of N atoms, this potential energy is a function of $3N$ cartesian coordinates or $3N-6$ internal coordinates. The minima of the PES are of interest because these are the energies for which the atoms of the molecule are in a stable state. Moving away from these minima in any direction the potential energy is larger. Finding the minima is easier when knowing the curvature of the PES, which is the second derivative of the potential energy for each individual coordinate. These second derivatives can be gathered in the *Hessian matrix*:

$$\mathbf{H} = \begin{bmatrix} \frac{\partial^2 E}{\partial x_1^2} & \frac{\partial^2 E}{\partial x_1 \partial x_2} & \cdots & \frac{\partial^2 E}{\partial x_1 \partial x_{3N}} \\ \frac{\partial^2 E}{\partial x_2 \partial x_1} & \frac{\partial^2 E}{\partial x_2^2} & \cdots & \frac{\partial^2 E}{\partial x_2 \partial x_{3N}} \\ \cdots & \cdots & \ddots & \cdots \\ \frac{\partial^2 E}{\partial x_{3N} \partial x_1} & \frac{\partial^2 E}{\partial x_{3N} \partial x_2} & \cdots & \frac{\partial^2 E}{\partial x_{3N}^2} \end{bmatrix}. \tag{2.20}$$

When the eigenvalues of the Hessian are all non-negative, the solution is a

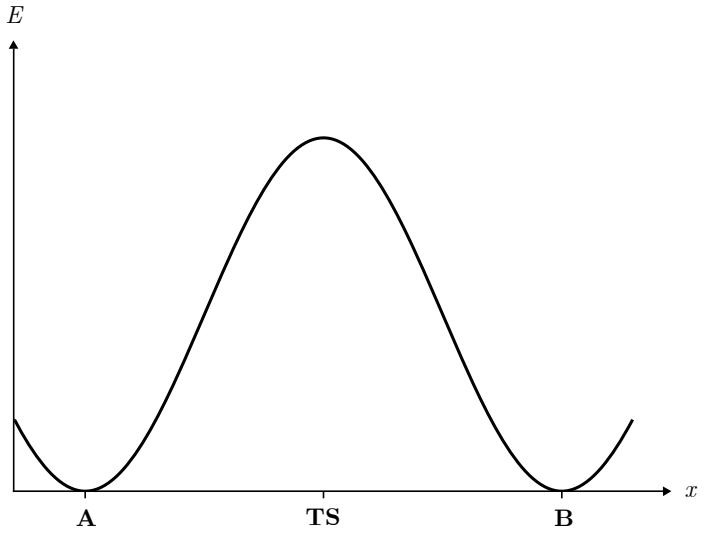

Figure 2.2: One-dimensional figure of two local energy minima, **A** and **B**, and the transition state (**TS**) that connects them.

local minimum [21, p. 272]. One or more negative eigenvalues gives a local maximum [22]. The most interesting path between two local minima is called the *minimum energy path* and passes through a first order saddle point called the transition state (TS), illustrated in Figure 2.2 [9, p. 134]. The Hessian matrix for the transition state has exactly one negative eigenvalue. This is the point with the largest energy on the path. The energy cost to get from one minimum to the transition state is called the *activation energy* (E_a). Going from **A** to **B**, this energy is defined as

$$E_{\mathrm{a}} = E(\mathbf{TS}) - E(\mathbf{A}), \tag{2.21}$$

where $E(\mathbf{TS})$ is the energy at the transition state, and $E(\mathbf{A})$ is the energy at **A**. With $\mathbf{M}_{ij} = m_i \delta_{ij}$, the mass-weighted Hessian is:

$$\mathbf{F} = \frac{1}{\sqrt{m_i}} \frac{\partial^2 E}{\partial x_i \partial x_j} \frac{1}{\sqrt{m_j}}. \tag{2.22}$$

The mass-weighted Hessian matrix has $3N$ eigenvectors, $\mathbf{e}_i$, with corresponding eigenvalues, λ_i, which have to satisfy:

$$\mathbf{F}\mathbf{e}_i = \lambda_i \mathbf{e}_i. \tag{2.23}$$

Hence, the characteristic vibrational frequency of the bond length oscillations is

$$\nu_i = \frac{1}{2\pi}\sqrt{\lambda_i}, \tag{2.24}$$

with $i = 1, 2, ..., 3N$. These vibrations are called *normal modes*. They are special solutions to equation (2.23) and describe the vibrations in the molecule [9, pp. 114–118]. When calculating normal modes in DFT calculations, there is often a small numerical inaccuracy that may result in some low frequency vibrations being reported as imaginary [9, p. 127]. This is because of numerical errors when the Hessian matrix is calculated [23]. When vibrational frequencies are in bulk systems, they are called phonons [9, p. 127]. The vibrational frequencies calculated here are for $\mathbf{k} = 0$ [24, p. 78].

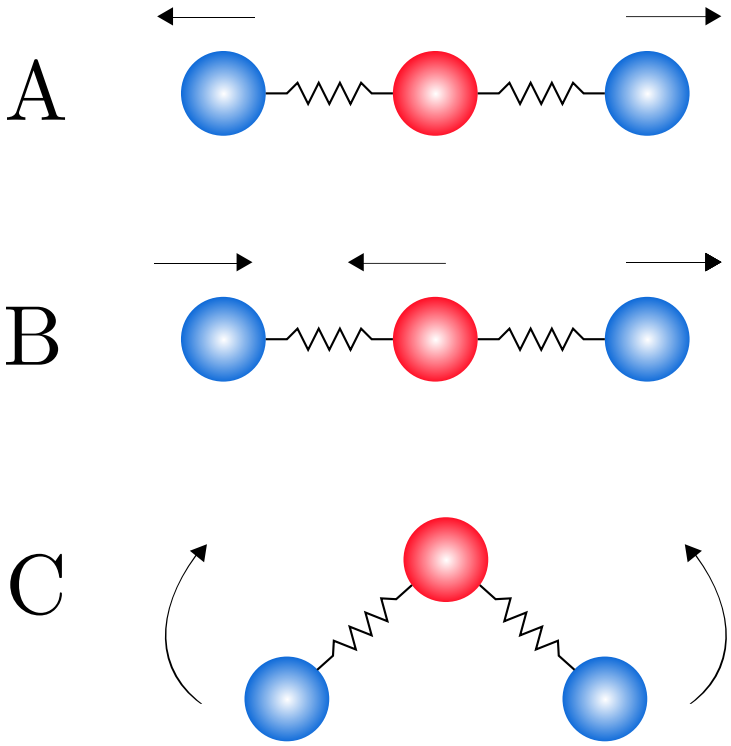

Figure 2.3: The different types of vibrational modes. Mode A is a symmetric stretch, B is the anti-symmetric stretch, and C is the degenerate bending mode.

A molecule has $3N$ degrees of freedom of motion, where 3 of them are for translation in three directions (x, y, z), and 3 for rotation around the three axes [25]. However, a linear molecule only has two modes of rotations as it does not rotate around its own axis. The remaining degrees of freedom are the vibrational degrees of freedom, for a non-linear molecule $3N-6$, and for a linear molecule $3N-5$. CO_2 is a linear molecule, hence it has $3 \times 3 - 5$ normal vibrations. The vibration modes are illustrated in Figure 2.3. Mode A in the figure, a symmetric stretch, is when carbon is at rest, and the two

oxygen atoms move away from carbon, in opposite directions at the same time. Mode B, an antisymmetric strech, is when the two oxygen atoms move in the same direction, and carbon moves in the opposite direction. Mode C is degenerate and is the two bending modes, moving perpendicular to the plane [25].

The vibrational modes can be measured by *Fourier transform infrared spectroscopy* (FTIR) [25, p. 2]. The symmetric stretch is a Raman active mode. In Raman spectroscopy, the vibrational frequency is measured as a shift from the incident beam frequency in the UV-region [25, p. 15]. This symmetric Raman mode will not be excited by electromagnetic waves. To get an oscillating electric dipole, it is necessary with an infrared (IR) active mode. These are found in the lab by looking at a sample and finding the amount of IR absorption [25, p. 13].

2.7 Density Functional Tight Binding

To do computations on large systems, it can be good to do cheap computations that are more efficient than DFT but still include quantum effects [26]. The DFTB computation method does this, using Bloch waves of a linear combination of atomic orbitals to look at the atomic states [17, p. 111]. This is a better approach for covalent bonded crystals than the free electron approach. With the single atom Hamiltonian

$$H_{\text{at}} = -\frac{\hbar^2\nabla^2}{2m_e} + V_{\text{at}}(\mathbf{r}), \tag{2.25}$$

where $V_{\text{at}}(\mathbf{r})$ is the atomic one-electron potential [17, p. 111]. The Hamiltonian for the solid becomes:

$$H_{\text{solid}} = H_{\text{at}} + \sum_{\mathbf{R}\neq 0} V_{\text{at}}(\mathbf{r}-\mathbf{R}). \tag{2.26}$$

Hence, the Hamiltonian of the solid is the Hamiltonian of an atom at the origin and the correction potential of all other atoms in the solid. The Hamiltonian only depends on the single atomic Hamiltonian and the interatomic distances in the molecule. This potential has the periodicity of the lattice.

Looking at neighbouring atoms that interact with each other, with the atomic wave function, ϕ_n, the wave function of the solid becomes:

$$\psi_{\mathbf{k}}(\mathbf{r}) = \frac{1}{\sqrt{N}} \sum_{\mathbf{R}} e^{i\mathbf{k}\cdot\mathbf{R}} \phi_n(\mathbf{r}-\mathbf{R}). \tag{2.27}$$

With

$$\gamma(\mathbf{R}) = -\int \phi_n^*(\mathbf{r}) \sum_{\mathbf{R}\neq 0} V_{\text{at}}(\mathbf{r}-\mathbf{R}) \phi_n(\mathbf{r}-\mathbf{R}) d\mathbf{r}, \tag{2.28}$$

it follows that the band structure then becomes

$$E(\mathbf{k}) = E_n - \beta - \sum_{\mathbf{R}\neq 0} \gamma(\mathbf{R}) e^{i\mathbf{k}\cdot\mathbf{R}}. \tag{2.29}$$

Here $-\beta$ is introduced because of the existence of other atom potentials, and it is a little shift in the atomic energy level. It is assumed that ψ is normalized. The wave functions are made up of Bloch waves and must therefore fulfill the Bloch theorem, Equation (2.4) [27, p. 32]. For atoms on a one-dimensional chain separated with a distance a, the energy for spherically symmetric s-orbitals becomes [17, p. 114]

$$E_s(\mathbf{k}) = E_s - \beta_s - 2\gamma_s \cos(ka). \tag{2.30}$$

The energy is the smallest for $k = 0$ and largest for $k = \pi/a$, that is, at the boundaries of the Brillouin zone. An atom put together of several orbitals will give rise to several bands for the various orbitals, a band per orbital. The width of the band is given by $4\gamma_s$. The difference between the bands for the various orbitals will give rise to a band gap. The band gap will separate an empty band at the top and a full band at the bottom. This gap will increase when the interatomic distance decreases. When the band gaps overlap, the collection of atoms at hand is a metal [27, p. 37]. In the opposite case, when the band gap is large, it is an insulator.

By combining the tight binding model with DFT one gets DFTB. Hence DFTB is an approximation of the Kohn–Sham method. In standard DFTB, the total energy is not calculated iteratively because it does not include the fluctuations of the energy density [28].

The DFTB method has several Hamiltonians, and the two used in this thesis are SCC-DFTB and GFN1-xTB. SCC-DFTB is the self consistent charge-correction. Here the fluctuations of the energy density are calculated, as op-

posed to normal DFTB calculations [28, 29]. The SCC-DFTB Hamiltonian is based on the theory of the Slater–Koster technique. This type of DFTB calculations reduces the linear algebra operations and can store integrals [30]. GFN1-xTB is the Grimme version of extended tight-binding and is also self consistent [30]. It is similar to the SCC-DFTB Hamiltonian, but it does not store integrals in the same way. It makes use of Slater-type orbitals. Also, this Hamiltonian makes use of an extended Hückel-like approximation [30].

2.8 K-Space Sampling

In DFT and DFTB calculations, a function on the form

$$\bar{g} = \frac{\mathrm{V_{cell}}}{(2\pi)^3} \int_{\mathrm{BZ}} g(\mathbf{k}) d\mathbf{k} \tag{2.31}$$

is evaluated by dividing it into smaller parts and evaluating them in a set number of discrete points. The individual parts are then summed together to find a result close to the true integral [9, p. 53]. Using more k-points gives a numerical convergence closer to the exact integral and hence better accuracy. However, it also requires more computer time [31, 32].

The number of k-points in each direction in the reciprocal space has to be specified in the computations. With three identical lattice vectors and M k-points per lattice vector, the total amount of k-points for the calculation is $M \times M \times M$ [9, pp. 55–59]. The density of k-points should be equal in all directions, which means that if lattice vector $|\mathbf{a}_1| > |\mathbf{a}_2|$, then $M_1 < M_2$. This method was developed by Monkhorst and Pack in 1976 [33]. A good way to save computation time is to see that the Brillouin zone is symmetric, and hence use fewer k-points. A convergence test can be conducted to check the accuracy of the results. They are said to be well converged when the energy is independent of the number of k-points [9, p. 55].

2.9 Dispersion Correction

Weak forces, like the van der Waals forces, are not taken into consideration in the DFT calculations. These forces are important in weakly bonded systems, for example in layered structures as clay, and arise from electron interactions [9, p. 225]. The dispersion between two spherically symmetric atoms, with r the distance between the atoms, and other physical constants, C, is

$$V^{\text{dispersion}} = -\frac{C}{r^6}. \tag{2.32}$$

Stefan Grimme et al. developed a method to include the dispersion correction in DFT calculations in the early 2000s [34]. It was named DFT-D3, and in 2010 this was renewed for a more accurate version, D4 [35]. The D4 dispersion correction is dependent on the atomic charges. The energy for DFT-D3 is

$$E_{\text{DFT-D3}} = E_{\text{KS-DFT}} + E_{\text{disp}}, \tag{2.33}$$

where $E_{\text{KS-DFT}}$ is the Kohn–Sham energy, and E_{disp} is the dispersion energy, which has the following form [34, 35]

$$E_{\text{disp}} = \sum_{AB} \sum_{n=6,8,10\ldots} s_n \frac{C_{(n)}^{AB}}{R_{AB}^{(n)}} f_{\text{damp}}^{(n)}(R_{AB}). \tag{2.34}$$

Here, AB denotes an atom pair, with $R_{AB}^{(n)}$ the distance between these atoms, and s_n is a scaling factor. The damping factor, $f_{\text{damp}}^{(n)}(R_{AB})$, is included to avoid singularities for $R_{AB}^{(n)}$ close to zero. The n-th order dispersion coefficient, $C_{(n)}^{AB}$, is calculated recursively from the Casimir–Polder integration. With $\alpha(i\omega)$ as the atomic polarizabilities, the first coefficient is:

$$C_6^{AB} = \frac{3}{\pi} \int_0^\infty d\omega \; \alpha^A(i\omega)\alpha^B(i\omega). \tag{2.35}$$

For SCC-DFTB, computations can be done with or without empirical van der Waals potentials [28]. For the Hamiltonian GFN1-xTB, the dispersion correction energy is a part of the total energy, and hence the weak van der Waals forces are included in this Hamiltonian [34, 30]

Chapter 3

Computational Details

In this project, the calculations were done with DFT and DFTB, using the quantum chemistry program Amsterdam Modelling Suite (AMS) from Software for Chemistry & Materials (SCM) [36, 37, 38, 39]. For the clay calculations in DFT, the periodic BAND program was used [40, 41]. For non-periodic atoms and molecules, Amsterdam Density Functional (ADF) was used. The ADF program uses a combination of slater type orbitals (STO) and natural atomic orbitals (NAO) [42].

Throughout the thesis, DFTB computations were done on the Linux cluster at the Department of Physics running five processes in parallel per job. The more demanding DFT computations were performed on the NTNU IDUN computing cluster [43]. The cluster has more than 70 nodes and 90 GPGPUs. Each node contains two Intel Xeon cores, at least 128 GB of main memory, and is connected to an Infiniband network. Half of the nodes are equipped with two or more Nvidia Tesla P100 or V100 GPGPUs. Idun's storage is provided by two storage arrays and a Lustre parallel distributed file system. The DFT computations were done running 20 processes in parallel per job.

The amount of CO_2 captured in fluorohectorite depends on the cation in the interlayer. Calculations were done to see how many molecules of CO_2 could fit in fluorohectorite with group I cations Li^+, Na^+, K^+, Rb^+ and Cs^+, group II cations Be^{2+}, Mg^{2+}, Ca^{2+} and Ba^{2+}, as well as the transition metal Ni^{2+}. By looking at the energy differences, it is possible to predict if CO_2 will bind to a system of fluorohectorite or not. In this project, the reaction energy, ΔE, is defined as

$$\Delta E = E_{\text{product}} - E_{\text{reactants}}, \tag{3.1}$$

and is seen as larger the more negative it is. It was also of interest to see what

orientation in space the molecules will have and hence how big the bond length will be. The bond length $d_{X–O}$ is taken as the average distance between the cation, X, and the closest oxygen atom of CO_2 molecules. In the formation of CO_3, the bond length $d_{C–O}$ is taken as the distance between the carbon in CO_2 and the closest oxygen in the fluorohectorite.

One way to reduce the required computational power is to simulate the problem at hand with an effective ion core where several electrons are included, known as the *frozen core approximation*. Trying to simulate all electrons in a molecule gives a lot of variables. Using less electrons in the calculations will not necessarily mean less physical accurate calculations. This is because the electrons closest to the ion core often do not interact with other electrons and can be seen as an effective frozen core. By using a large frozen core, one looks at the problem as if most of the electrons in the problem are part of the ion core. This reduces the required computational power considerably, but it is not a good physical representation of electrons in a material. On the contrary, using a small frozen core, only the innermost electrons are looked upon as part of the ion core. This requires more computational power than a large frozen core.

Choosing the correct basis set will have an impact on the computational time, memory usage and accuracy of the calculations. Basis sets with less information will reduce the computational time, but will also include less information about the physical system. The basis sets have different sizes. For STO orbitals these are single-, double-, and triple-zeta, and they come with or without polarization functions.

For all DFT calculations, geometry optimization was used with the same settings. The numerical quality can be set to Basic – Normal – Good – Very Good – Excellent. For these calculations Good was used. The XC functional used was the GGA revPBE. The frozen core can be set to Large – Medium – Small, which reflects the amount of atomic orbitals frozen to the core. It was here set to Medium. The basis set used was triple zeta polarization (TZP). These DFT calculations will be referred to as *revPBE*. Some DFT calculations took the van der Waals forces into account, using the Grimme3 BJDAMP dispersion correction. These calculations will be referred to as revPBE Grimme.

For ADF calculations on single atoms or molecules, the settings were a little different from the BAND calculations. The numerical quality can be set to Basic – Normal – Good – Very Good – Excellent. For these calculations, Good

was used. The frozen core can be set to Large – Small – None. It was here set to Small. The same XC functional and basis sets were used as for the BAND calculations, namely GGA revPBE, and TZP. Hence, these calculations will also be referred to as revPBE calculations.

In the SCC-DFTB calculations, we use the QUASINANO2015 parameter set, restricted to elements H to Ca [44]. GFN1-xTB supports all atoms up to radon, but this method fails for 3D periodic systems. Hence, only slab calculations were done with this Hamiltonian. For both Hamiltonians in DFTB, the numerical quality of the k-space integration can be set to GammaOnly – Basic – Normal – Good – VeryGood – Excellent. For these calculations, Good was used. For all DFT and DFTB calculations, the frequencies and normal modes of vibrations were calculated. For both SCC-DFTB and GFN1-xTB, there was a stronger emphasis on geometries than chemical reaction energies in the parametrization [45, 44]. As a consequence, we expect geometries to be more reliable than reaction energies in our calculations.

In this project, several models were used to meet different needs. DFT revPBE and revPBE Grimme were of interest, but would be too time consuming. SCC-DFTB is a good model for organic materials and can model bulk structures, but it can not accommodate for all atoms. Especially nickel is of interest because of experimental results. Hence, GFN1-xTB was used to model atoms which were not possible with SCC-DFTB, but this model does not support slab computations. Hence, GFN1-xTB was applied to slab models of Ni-Fh.

To exemplify the time difference between DFT and DFTB calculations, two identical jobs were done with SCC-DFTB and revPBE, both without dispersion correction. Both were run on the same computer with five processes in parallel per job. Doing DFTB computations gives an elapsed time of 73.42 seconds. The results from DFT took 72033.24 seconds, which is a factor of 1000 more.

The simulation has converged when the convergence criteria are reached. For the simulations in this project, the default criteria in the ADF program were used when finding the energy minima: for the change in the energy from one geometry to the next, 10^{-3} Hartree; for the change in nuclear gradients, 10^{-3} Hartree/Angstrom; for the step size from a converged geometry, 10^{-3} Angstrom; and for the threshold for optimizing the lattice vectors, $5{\cdot}10^{-4}$ Angstrom [46].

3.1 Optimization Methods

An important geometry optimization algorithm of the DFTB and DFT calculations is the fast inertial relaxation (FIRE). This is a good method for big systems with more than 1000 atoms and hence thousands of degrees of freedom [46]. It uses molecular dynamics to decide the atomic displacements from one geometry to the next. The gradient of the energy is used as the convergence criteria. This is opposed to other methods like the large scale Broyden–Fletcher–Goldfarb–Shanno (L-BFGS) and conjugate gradient (CG), which are quasi-Newton methods and use the change in energy, the change of geometry and the change of the energy gradient as the convergence criteria [47, 48]. It is a simple but fast method that does not require a lot of memory. The time of the calculations only depends on the engine performance [46]. Also, it works well for coordinate constraints, fixed atoms constraints, and for lattice optimization and coordinate constraints.

Chapter 4

Results and Discussion

To investigate the possibility of CO_2 storage in fluorohectorite, several simulations were done with DFT and DFTB to see how CO_2 binds to various cations in fluorohectorite. The cations used were Li^+, Na^+, K^+, Rb^+, Cs^+, Ca^{2+}, Ba^{2+} and Ni^{2+}. Lab experiments show that especially Ni^{2+}, Li^+ and Na^+ are good for adsorbing CO_2 [12]. Simulations were also done for Be^{2+} and Mg^{2+} to look at trends within periodic groups and for atom sizes. The binding energy, ΔE, and the basal interlayer distance, d_{001}, were found for all systems, together with the bond lengths between the cation and the closest oxygen of the CO_2 molecules, $d_{\text{X–O}}$. The lattice vectors for plain fluorohectorite can be seen in Figure 4.1.

The basal interlayer distance and $|\mathbf{a}_3|$ are the same when the angles α and β are approximately 90°. With SCC-DFTB calculations, these angles are: 80.22°< α < 99.85°, 81.80°< β < 92.43°, and 89.07°< γ < 91.02°, which in this case is seen as "close enough". The smallest values for $|\mathbf{a}_1|$ and $|\mathbf{a}_2|$ are 9.63 Å and 5.55 Å, respectively. The largest values are 10.26 Å and 5.96 Å, respectively. With GFN1-xTB slab calculations, the angle is 89.71°< α < 91.23°, while 7.91 Å < $|\mathbf{a}_1|$ < 9.03 Å and 4.57 Å < $|\mathbf{a}_2|$ < 5.23 Å. With revPBE calculations, the angles are 89.85°< α < 92.43°, 88.87°< β < 93.37° and 90°< γ < 90.54°, and $|\mathbf{a}_1| \simeq 8.97$ Å and $|\mathbf{a}_2| \simeq 5.18$ Å.

Discussions with the experimental group working with fluorohectorite at the Department of Physics at NTNU influenced the chosen number of CO_2 molecules used in the computations. Their results typically give a mass increase of around 9 %, which means an uptake of 1-2 molecules of CO_2 per unit cell [49]. Results from Cavalcanti et al. can indicate that fluorohectorite may be able to adsorb more [50]. Consequently, it is natural to examine structures

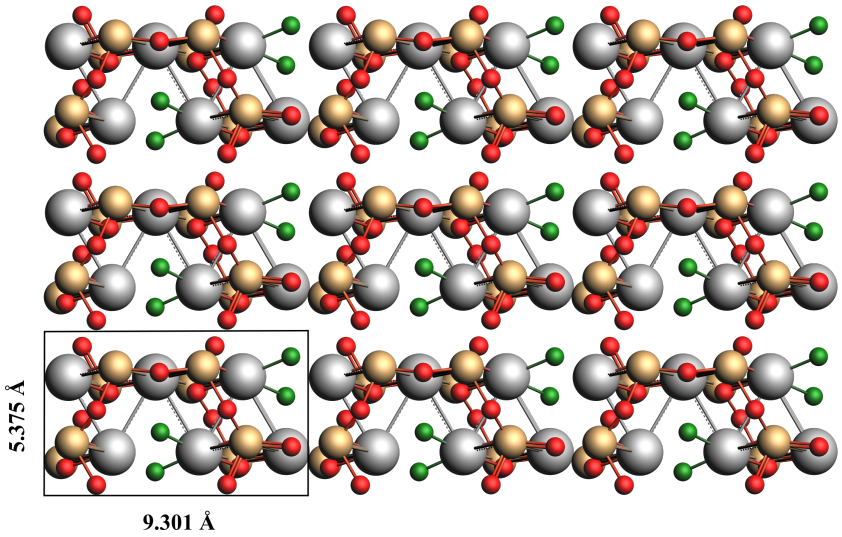

(a) Fluorohectorite in the xy-plane with $\mathbf{a}_1$ and $\mathbf{a}_2$. The values are for plain fluorohectorite. (revPBE).

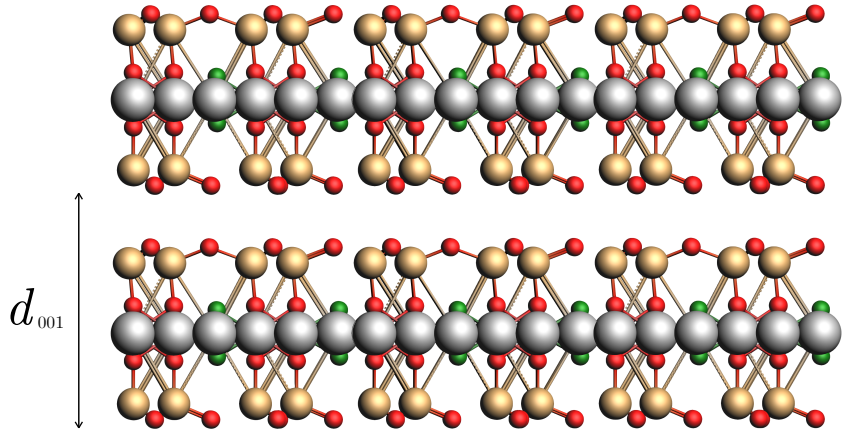

(b) Fluorohectorite in the xz-plane with d_{001} indicated.

Figure 4.1: Fluorohectorite. Color code: Mg = gray; F = green; O = red; Si = gold. Figure made in Amsterdam Modelling Suite.

containing up to 3 CO_2 molecules per unit cell.

In this chapter, there are three main sections. Firstly, DFT and DFTB will be compared with respect to reaction energies, the basal interlayer distance, and the X–O distance. Computations were done on a small selection of single cations and 1 CO_2, and then all the models were applied to 2Li-Fh. Secondly, the two DFTB methods are used to look at various structures with cations and CO_2 in fluorohectorite. Finally, vibrational frequencies associated with the intercalated CO_2 molecules are presented.

4.1 DFT vs. DFTB

Going into this project, the results from the specialization project were in mind, illustrated in Figure 4.2. When looking at single cations and various amounts of CO_2 with revPBE, nickel was the best cation in terms of binding to CO_2, while cesium was the least promising candidate. In general, smaller cations and cations with a higher valence were found to make the strongest bonds to CO_2.

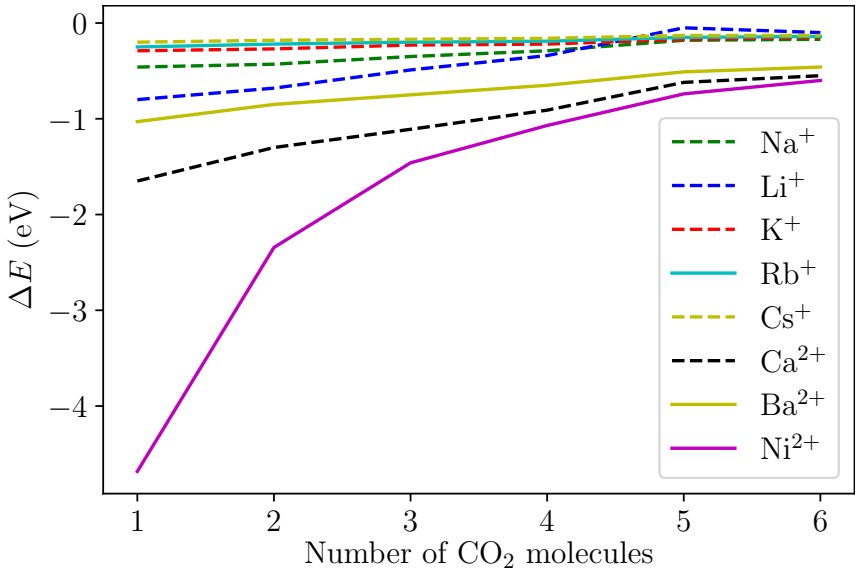

Figure 4.2: The results from computations in the specialization project last autumn. Reaction energy for single cations with various amounts of CO_2. (revPBE).

Computations were done on four single cations with 1 CO_2 with the three models revPBE, SCC-DFTB and GFN1-xTB. The results can be seen in Table 4.1. For revPBE and GFN1-xTB, nickel has the largest reaction energy out of the four cations, and lithium has larger energies than sodium. Hence GFN1-xTB follows the same pattern as revPBE from the specialization project. However, for SCC-DFTB, out of the three cations that could be simulated, lithium has the largest reaction energy.

In computations with fluorohectorite systems, SCC-DFTB and GFN1-xTB give some different results than revPBE. Mainly giving the same trend as for single cations and CO_2, bonding less strongly for more amounts of CO_2. The revPBE computations are time consuming and could not be applied to all the different cations in fluorohectorite. Therefore, geometry optimizations for various cations and a number of CO_2 in fluorohectorite were done with SCC-DFTB and GFN1-xTB. However, it is interesting to see how "good" these models are compared to revPBE for one specific type of cation. These com-

Reaction	revPBE		SCC-DFTB		GFN1-xTB	
	ΔE (eV)	$d_{X–O}$ (Å)	ΔE (eV)	$d_{X–O}$ (Å)	ΔE (eV)	$d_{X–O}$ (Å)
$Li^+ + CO_2$ –> $(LiCO_2)^+$	−0.80	1.87	−2.90	1.55	−1.26	1.77
$Na^+ + CO_2$ –> $(NaCO_2)^+$	−0.46	2.32	−1.08	2.24	−0.66	2.13
$Ca^{2+} + CO_2$ –> $(CaCO_2)^{2+}$	−1.65	2.21	−1.12	2.65	−3.35	2.04
$Ni^{2+} + CO_2$ –> $(NiCO_2)^{2+}$	−4.68	1.94	–	–	−10.62	1.75

Table 4.1: Reaction energy and X–O bond distance for single cations and 1 CO_2. Comparison of DFT and DFTB methods. SCC-DFTB only supports elements H to Ca.

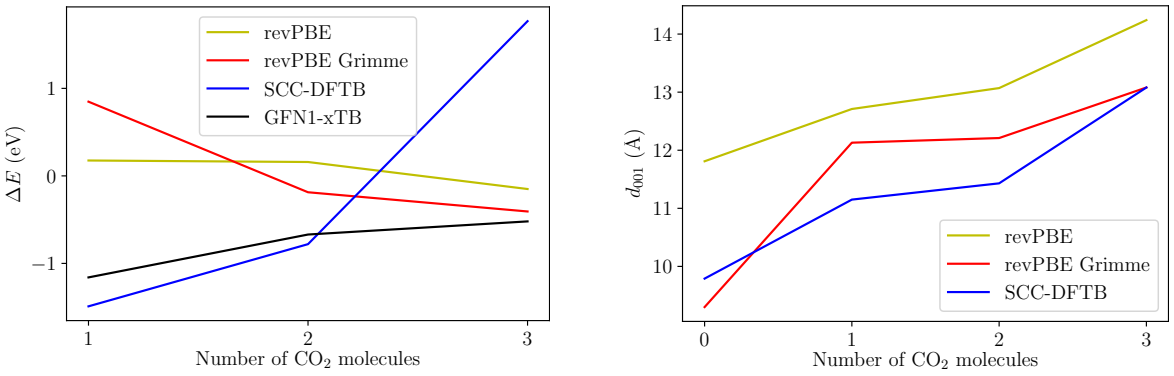

(a) **(b)**

Figure 4.3: (a) Reaction energy, and (b) basal interlayer distance with 1, 2 and 3 intercalating CO_2 for 2Li-Fh done with various computation methods.

putations were done to see how the trend differs between the three types of computation methods. The type of cation is here 2Li-Fh (see Section 1.3 and Equation (1.1) for the abbreviations). One series was done with revPBE, and one for revPBE with the Grimme dispersion correction.

Looking at the reaction energies for these four methods in Figure 4.3a and in Table 4.2, the trends are quite different. SCC-DFTB and GFN1-xTB follow the trend expected from computations with only cations and CO_2 seen in Figure 4.2, namely that the reaction becomes less favorable when adding more CO_2 to the system. For 3 CO_2 in SCC-DFTB, the reaction energy is endothermic, with $\Delta E = 1.77$ eV from 2 to 3 CO_2. For both revPBE methods, the reaction becomes more favorable the more CO_2 is added. We expect calculations done with revPBE to be more accurate than DFTB calculations. These results suggest it is difficult to accommodate 1 CO_2, but then the first CO_2 makes room for more CO_2.

The general trend for d_{001} is that it increases with an increasing amounts of CO_2 added, which means clay swelling, seen in Figure 4.3b and Table 4.2. However, for all three methods, going from 1 to 2 CO_2 does not increase

	revPBE			revPBE Grimme			SCC-DFTB			GFN1-xTB		
# CO_2	ΔE (eV)	d_{001} (Å)	d_{X-O} (Å)	ΔE (eV)	d_{001} (Å)	d_{X-O} (Å)	ΔE (eV)	d_{001} (Å)	d_{X-O} (Å)	ΔE (eV)	d_{001} (Å)	d_{X-O} (Å)
0	-	11.91	-	-	9.30	-	-	9.79	-	-	-	-
1	0.10	12.71	3.76	0.85	12.13	4.48	-1.46	11.15	1.67	-1.17	-	-
2	0.16	13.07	2.86	-0.19	12.21	2.84	-0.78	11.43	2.02	-0.67	-	3.64
3	-0.15	14.24	4.17	-0.41	13.08	3.71	1.77	13.08	4.13	-0.52	-	3.33

Table 4.2: Reaction energies, basal interlayer distances and average X–O bond distances for 2Li-Fh. Comparison of DFT and DFTB methods. See Figure 4.4 for the geometry of the products with 3 CO_2. GFN1-xTB are slab calculations.

d_{001} much. This might be because the unit cell has two cations in the interlayer. Adding another CO_2 to an existing CO_2 makes the geometry symmetric, which might be favored. Cavalcanti et al. reported a d_{001} of 10.3 Å with no CO_2, and 11.9 Å with 2.3 CO_2 per unit cell [50][1]. All methods are qualitatively in agreement with these experimental results.

The basal interlayer distance is quite similar for revPBE Grimme and SCC-DFTB, as they are both ca. 13 Å for 3 CO_2, and they start at 9.3 Å and 10.3 Å, respectively. It is larger for revPBE than the other two for all number of CO_2 added. The basal interlayer distance is larger for revPBE than for revPBE Grimme, which was expected because of the van der Waals forces pulling the sheets together. In general, the X–O bond distance increases with increasing amounts of CO_2. However, for revPBE and revPBE Grimme, CO_2 comes closer to the interlayer cations when adding 2 CO_2, and then $d_{X–O}$ increases when adding the third CO_2.

Looking at Figure 4.4, the geometries for the four methods are quite similar. The lithium atoms are placed inside the tetrahedral sheet of oxygen and silicon, often referred to as the hexagonal cavity [51]. For the SCC-DFTB and revPBE Grimme geometries, all three CO_2 are placed quite similarly, namely a somewhat parallel orientation to the fluorohectorite layers. Parallel orientation of the CO_2 seems to be the most optimal orientation because of the cation charge on the clay surface [5, p. 112].

When the distance between the clay layers increases, the CO_2 alignment tends to change from parallel to somewhat tilted, which also has been seen experimentally [5, p. 112]. This seems to support the results from revPBE vs. revPBE Grimme. The former has a larger distance between the layers, seen from Figure 4.3b, and also more of an angle to CO_2 than for revPBE Grimme. However, this angle of CO_2 only applies to the last of 3 CO_2 to be added to the system. Because the revPBE Grimme takes the van der Waals forces into account, this is thought to be a more realistic model for a clay material [5, p. 180]. When adding dispersion correction to the SCC-DFTB model, the van der Waals forces pull the sheets together, observing that d_{001} is slightly smaller with dispersion correction than without it, as expected.

In the slab calculations with GFN1-xTB, there is some tendency of formation of CO_3 entities upon reaction between a CO_2 molecule and an oxygen atom in the clay surface (Figure 4.4d). Although we have not found any experimental

[1] For lithium, where Cavalcanti et al. use $y = 1.2$ in Equation (1.1).

evidence in the literature, we believe that CO_3 groups cannot be ruled out in these systems. Whenever present, they should be easily visible in FTIR spectroscopy, see Section 4.3.

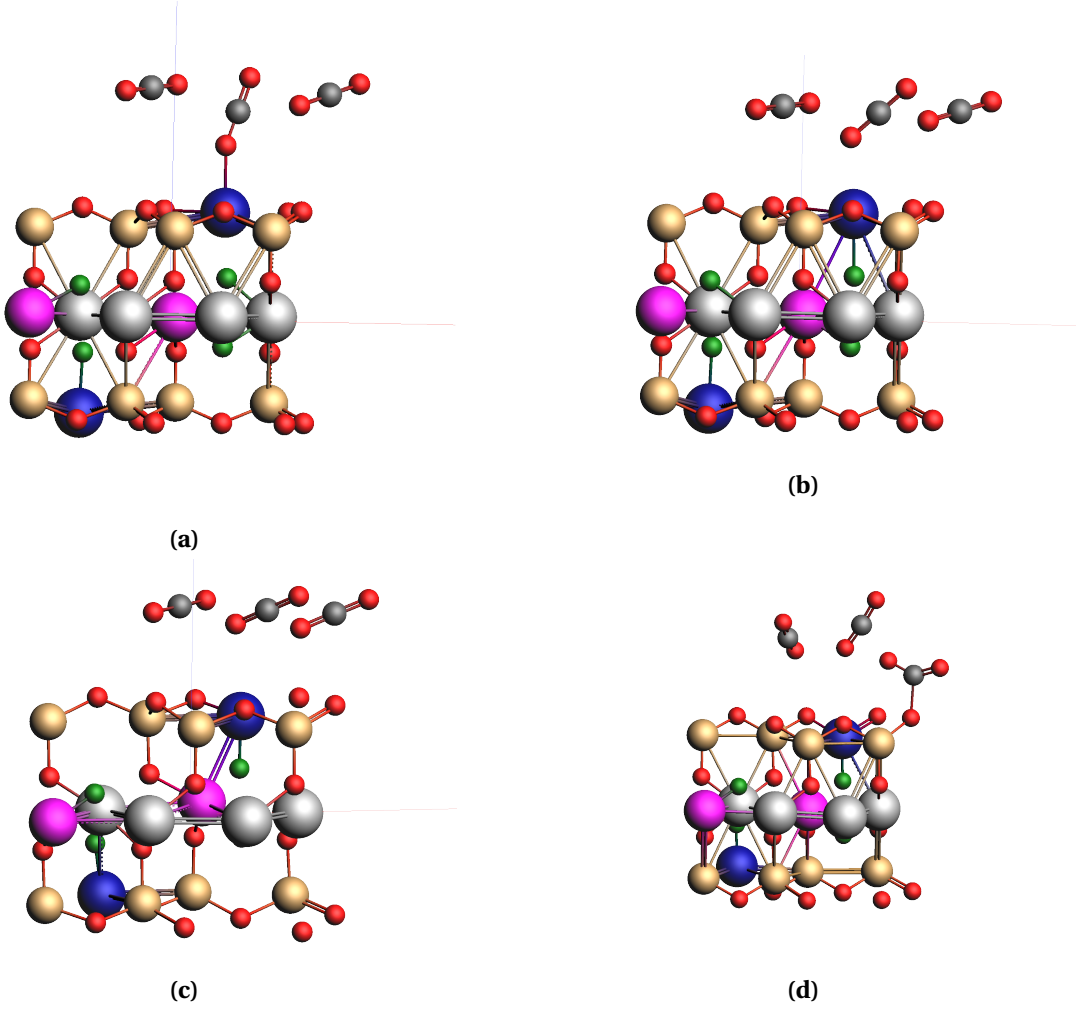

Figure 4.4: Geometry of the unit cell of 2Li-Fh together with 3 CO_2 for (a) revPBE, (b) revPBE Grimme, (c) SCC-DFTB, and (d) GFN1-xTB. (Mg = gray; F = green; O = red; Si = gold; Li = purple; C = black; X = blue; here X = Li.)

4.2 Geometries and Energies

4.2.1 SCC-DFTB

# CO_2	Li-Fh	Na-Fh	K-Fh	2Li-Fh	2Na-Fh	2K-Fh	Be-Fh	Mg-Fh	Ca-Fh
1	−0.91	−0.25	−0.22	−1.46	1.76	0.54	−0.35	−0.36	0.57
2	−0.24	−0.35	−0.82	−0.78	−1.12	−1.05	−0.77	−0.63	0.05
3	0.02	−0.06	−0.19	1.77	−0.12	−0.28	−0.33	−0.35	−0.40

Table 4.3: Reaction energy ΔE (eV) for adsorption of the first three CO_2 molecules with one and two cations pr unit cell. (SCC-DFTB.)

# CO_2	Li-Fh	Na-Fh	K-Fh	2Li-Fh	2Na-Fh	2K-Fh	Be-Fh	Mg-Fh	Ca-Fh
1	4.31	2.40	2.66	1.67	2.41	2.72	1.31	2.01	3.51
2	4.42	2.39	2.65	2.02	2.40	2.72	1.43	3.17	2.80
3	4.09	3.37	2.65	4.13	3.28	2.65	3.96	3.55	2.85

Table 4.4: Bond distances $d_{X–O}$ (Å) with up to three adsorbed CO_2 molecules with one and two cations pr unit cell. (SCC-DFTB.) For 2X-Fh: average of two X–O distances.

# CO_2	Li-Fh	Na-Fh	K-Fh	2Li-Fh	2Na-Fh	2K-Fh	Be-Fh	Mg-Fh	Ca-Fh
0	11.82	10.70	11.30	9.79	10.18	11.26	12.60	12.02	10.40
1	12.81	12.39	12.29	11.15	12.13	12.22	12.12	12.59	11.67
2	12.78	12.75	12.48	11.43	12.66	12.49	12.14	12.59	12.58
3	12.82	12.60	13.81	13.08	12.51	12.77	12.72	12.47	12.77

Table 4.5: Basal interlayer distance d_{001} (Å) with up to three adsorbed CO_2 molecules with one and two cations pr unit cell. (SCC-DFTB.)

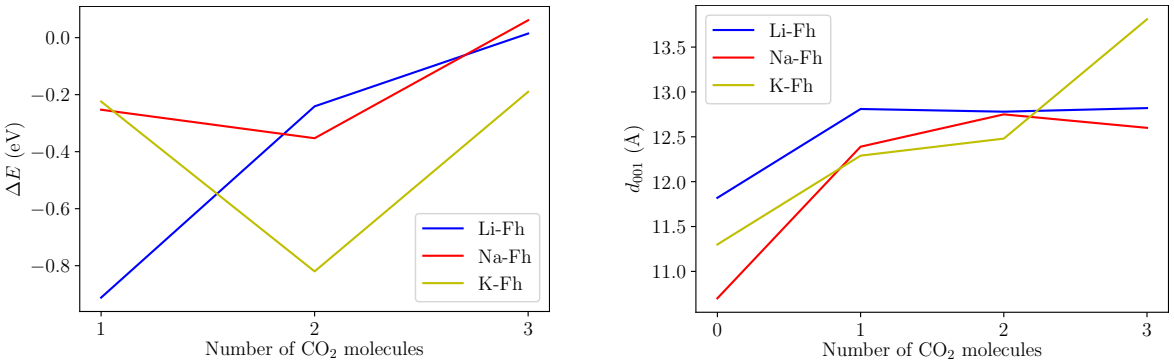

(a) **(b)**

Figure 4.5: (a) Reaction energy and (b) basal interlayer distance with 1, 2 and 3 intercalating CO_2 molecules and one group I interlayer cation. (X = Li, Na, K). SCC-DFTB calculations.

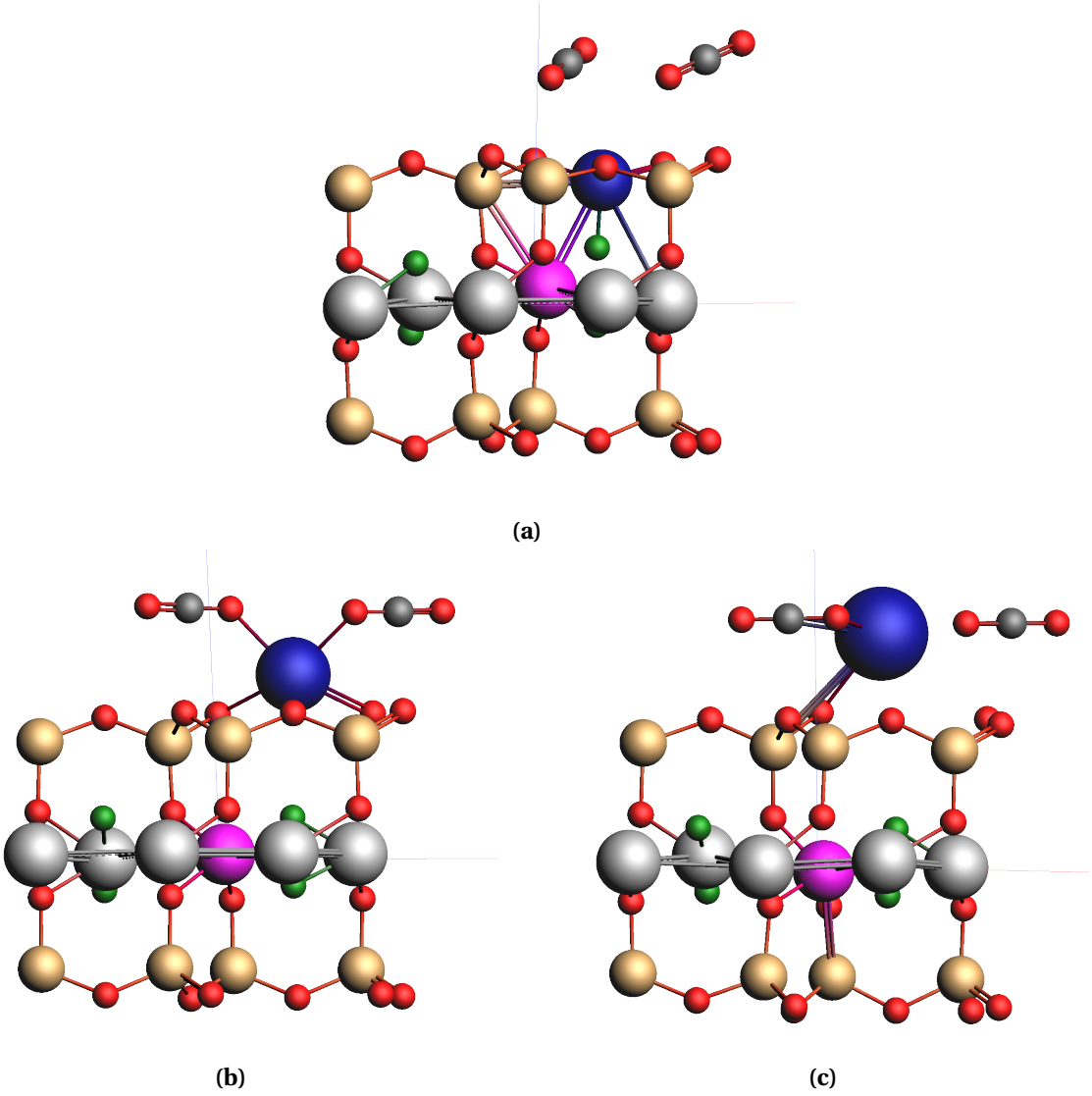

(a) **(b)** **(c)**

Figure 4.6: SCC-DFTB geometry of the unit cell and 2 CO_2 for (a) Li-Fh, (b) Na-Fh and (c) K-Fh. (Mg = gray; F = green; O = red; Si = gold; Li = purple; C = black; X = blue.)

One group I interlayer cation

The reaction energies for one group I cations in the interlayer, Li-Fh, Na-Fh and K-Fh, are illustrated in Figure 4.5a and can be seen in Table 4.3. At first sight, it would seem intuitive that it should become more difficult the more CO_2 one tries to add into the clay, and hence that the reaction energy for Li-Fh is the most correct. However, for larger amounts of CO_2, the reaction energy is larger for the larger cations potassium and sodium. This is in agreement with results from Cavalcanti et al. [50]. We suggest that this is mainly due to potassium and sodium being more exposed than lithium.

It looks like the CO_2 molecules for Li-Fh are closer to the oxygens in the clay layer than they are to the interlayer cation. Lithium is well packed into the

hexagonal cavity, illustrated by Li-Fh in Figure 4.6a, which has essentially the same geometry as with no CO_2. Because lithium is a small cation, and hence can fit into the hexagonal cavity, adding CO_2 means adding them to the vacuum layer of the clay, without it being able to bond much with the cation. This can also be backed by looking at the much larger values for $d_{X–O}$ in Table 4.4, where the values are larger for Li-Fh than for K-Fh and Na-Fh. Because the CO_2 molecules cannot access the cation, they will instead bond weakly with the other atoms in the clay, primarily the oxygen atoms.

For K-Fh and Na-Fh, the potassium and sodium cations are positioned more above the hexagonal cavity and not in it as for Li-Fh, seen in Figures 4.6b and 4.6c. This is also observed for sodium by Kalo et al. [51]. Hence CO_2 bonds to the cation rather than to the oxygen atoms in the clay. The CO_2 molecules are more bound to the cation for K-Fh and Na-Fh, with $d_{X–O}$ ca. 2.65 Å for potassium for all numbers of CO_2 and 2.40 Å for sodium, see Table 4.4. However, for Na-Fh it changes when adding the third CO_2. Two of the CO_2 molecules for Na-Fh are then, as for Li-Fh, positioned above an oxygen atom, with no bond to sodium, and $d_{X–O}$ increases to 3.37 Å. When the CO_2 molecules are further away from the cation, the reaction energy decreases, as seen for Na-Fh in Figure 4.5a.

Potassium is a larger cation and hence can accommodate more CO_2 than the smaller lithium and sodium. This seems to fit the explanation by Cavalcanti et al., where the larger cations can accommodate larger amounts of CO_2 [50]. From this it would be natural to suggest that potassium might be the best cation from these three because of the larger reaction energy for higher amounts of added CO_2. However, experimentally there is some disagreement if larger cations or smaller cations are the better CO_2 adsorbers. Loganathan et al. and Bowers et al. claim that larger cations are better [52, 53], while Seljelid claims small cations are better [12]. Loganathan et al. proposed that large cations are better because they should lower the energy barrier for adsorbing CO_2, and also that they result in a large basal interlayer spacing.

Looking at the changes in d_{001} in Figure 4.5b and Table 4.5, K-Fh and Na-Fh in general have smaller values than Li-Fh, even though lithium is better packed in the hexagonal cavity. When there is CO_2 added to the clay structures, this may be explained by the CO_2 that lies approximately parallel to the clay and hence takes up less space in the d_{001} direction, as for K-Fh and Na-Fh. For K-Fh, this changes when the third CO_2 is added and has a larger angle to the clay than for the other CO_2, hence gives a much larger value for d_{001}. The orienta-

tion of CO_2 for Li-Fh has an angle for all CO_2 and also larger values for d_{001}. In general, d_{001} should become larger when adding CO_2 to the clay material, and hence it seems reasonable that it becomes larger for larger amounts of CO_2 [50].

However, the larger d_{001} for Li-Fh does not necessarily make sense when there is no CO_2 present. Cavalcanti et al. found in experiments that Na-Fh has a larger interlayer separation than Li-Fh, and hence Na-Fh can hold more CO_2 than Li-Fh [50]. Assuming a larger interlayer separation means a larger d_{001}, it would be natural to assume that d_{001} should be larger for Na-Fh than for Li-Fh, which it is not here. The basal interlayer distance is the largest for Li-Fh and smallest for Na-Fh, with K-Fh in between. Hence the size of the atoms does not seem to be the reason, nor the position of the cation over the hexagonal cavity. The basal interlayer distance might be large for Li-Fh because lithium resides inside the hexagonal cavity, and hence the oxygen atoms at the top of one layer repel the oxygen atoms in the layer above.

Two group I interlayer cations

The reaction energies for two group I cations in the interlayer, 2Li-Fh, 2Na-Fh and 2K-Fh, are illustrated in Figure 4.7a and Table 4.3. As for Li-Fh, the reaction energy for 2Li-Fh decreases with increasing amounts of CO_2, and it would again seem intuitive that to be able to get 1 CO_2 into hectorite, one would first have to fit 1 CO_2 in. Hence that the reaction energy for 2Li-Fh would be the most correct of the three. However, the difference in trends may be explained by the geometry. 2Na-Fh without any CO_2, Figure 4.8c, is tightly bound and partly in the hexagonal cavity, but for 1 CO_2, Figure 4.8d, the cations are positioned above the hexagonal cavity. Hence it needs some activation energy to "pop" out of the cavity, and thus explain the positive reaction energy when adding 1 CO_2 for 2Na-Fh.

For 2Li-Fh, the two lithium cations start inside the hexagonal cavity, as for the geometry with 3 CO_2 seen in Figure 4.8b. For 1 and 2 CO_2 illustrated in Figure 4.8a, the cations "pop" out of the cavity and are situated above the cavity. Adding a third CO_2, the cations withdraw into the cavity again. The withdrawing cation can also explain the difference in X–O bond distance seen in Table 4.4. For 1 and 2 CO_2, this distance is at 1.72 Å and 2.31 Å. For 3 CO_2 this distance is 3.91 Å. When the cation is above the hexagonal cavity, it is more exposed and can hence bond with CO_2. As discussed for Na-Fh, the increase in $d_{X–O}$, meaning the CO_2 molecules are further away from the cation,

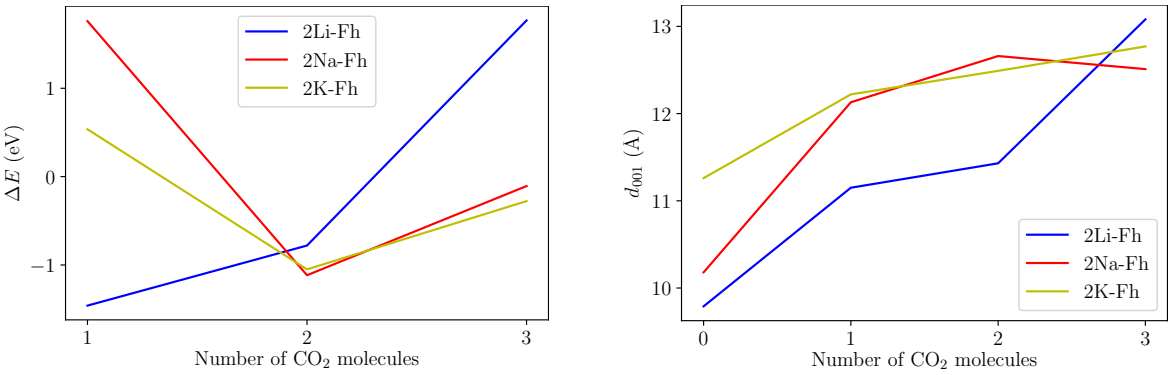

(a) **(b)**

Figure 4.7: (a) Reaction energy and (b) basal interlayer distance with 1, 2 and 3 intercalating CO_2 molecules and two group I interlayer cations. (X = 2Li, 2Na, 2K). SCC-DFTB calculations.

reduces the reaction energy for 2Li-Fh.

For 2 and 3 CO_2 the reaction energy is practically the same for 2Na-Fh and 2K-Fh. The d_{001}, seen in Figure 4.7b, and geometries, shown for Na-Fh in 4.8c and 4.8d, are also very similar in these cases. The difference is, as for K-Fh and Na-Fh earlier, that potassium is a larger cation and hence is a little bit more elevated above the hexagonal cavity for all number of CO_2. For 1 CO_2, potassium is positioned more above the hexagonal cavity than sodium. Hence 2K-Fh requires less energy for adding 1 CO_2 than 2Na-Fh. Adding the third CO_2 to 2K-Fh, d_{001} is increased. This is probably because the third CO_2 is still closely bonded with the cation, with $d_{X–O}$ = 2.65 Å, and hence to fit the new CO_2, d_{001} expands. For 2Na-Fh, adding the third CO_2 gives a slightly smaller d_{001} as the two sodium cations withdraw into the hexagonal cavity, and $d_{X–O}$ = 3.28 Å, which is an increase.

In general, the geometries, reaction energies and basal interlayer distance for one and two group I cations are quite similar. The trend of the energies are similar, but for two interlayer cations the reaction energy is positive for 1 CO_2 for 2K-Fh and 2Na-Fh and hence the reaction is predicted to be unlikely. This is also the case for 2Li-Fh with 3 CO_2. However, as mentioned in Chapter 3, the DFTB methods are expected to be more reliable for predicting geometries than reaction energies

The basal interlayer distance is in general smaller for 2Li-Fh than for Li-Fh, and the same goes for $d_{X–O}$. The largest difference between 2Li-Fh and Li-Fh are the geometries, where for 2Li-Fh the cations “pop” out of the hexagonal cavity as explained above. From this it would be natural to assume that the optimal geometry is for the cation to be positioned above the hexagonal

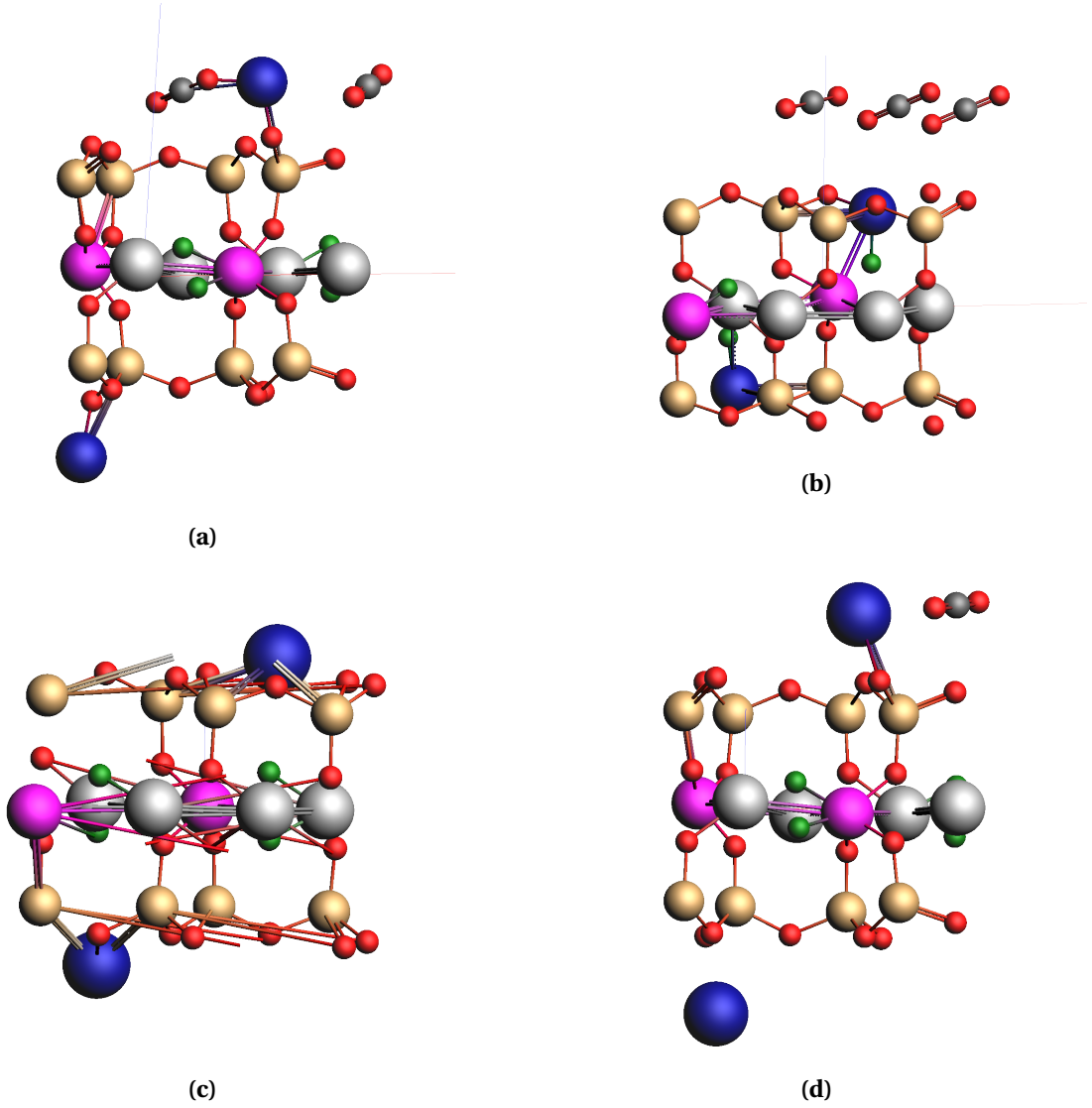

Figure 4.8: Geometry (SCC-DFTB) of the unit cell of fluorohectorite with 2 interlayer group I cations for (a) 2Li-Fh with 2 CO_2, (b) 2Li-Fh with 3 CO_2, (c) 2Na-Fh, and (d) 2Na-Fh with 1 CO_2. (Mg = gray; F = green; O = red; Si = gold; Li = purple; C = black; X = blue.)

cavity, so the CO_2 can bond with the cation, and hence give larger reaction energies and swelling.

Group II interlayer cations

The geometries for Ca-Fh are similar to the ones of K-Fh, which makes sense since the two cations have a similar size. As for K-Fh, calcium is positioned above the hexagonal cavity. However, the first CO_2 seems to position itself far away from the cation, with $d_{X–O}$ = 3.51 Å. The carbon in CO_2 is 2.66 Å away from the closest clay oxygen, which is probably the reason for the small reaction energy when adding 1 CO_2 to Ca-Fh. The distances from the cation to the CO_2 decrease when more CO_2 are added, and the energy is also in-

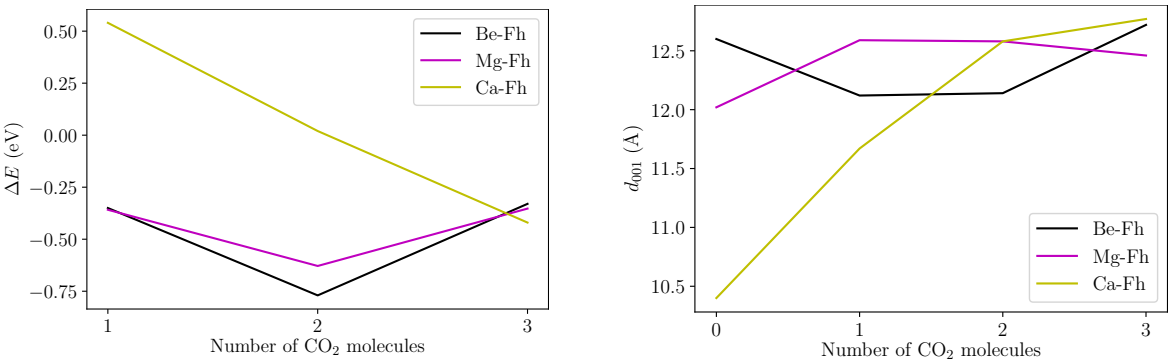

(a) **(b)**

Figure 4.9: (a) Reaction energy and (b) basal interlayer distance with 1, 2 and 3 intercalating CO_2 molecules and one group II interlayer cation. (X = Be, Mg, Ca). SCC-DFTB calculations.

creased, see Figure 4.9a and Table 4.3. However, the energy for Ca-Fh with 3 CO_2 is only barely larger than for Mg-Fh and Be-Fh. Maybe adding more CO_2 would prove Ca-Fh better for storing CO_2 in larger amounts. Looking at d_{001} for Ca-Fh in Figure 4.9b and Table 4.5, Ca-Fh clearly swells with added amounts of CO_2, as it should [50].

For Mg-Fh, the geometries are also similar to K-Fh and Ca-Fh, but the cation is placed inside the hexagonal cavity, like Li-Fh. As discussed for 2Li-Fh, the magnesium cation "pops" out of the cavity for 1 CO_2, but then goes back into the cavity for 2 and 3 CO_2. The distance from the cation to the CO_2 increases with an increasing number of CO_2, and the CO_2 are placed more in the vacuum layer than actually bonded to the cation. One CO_2 seems to bond with the cation while the other CO_2 are positioned ca. 3 Å above a clay oxygen.

Be-Fh is quite different than all other cations discussed so far. All geometries for Be-Fh are illustrated in Figure 4.10. As for Li-Fh, beryllium is a small atom and hence can fit into the hexagonal cavity. However, when 1 CO_2 is added, the cation "pops" out of the cavity, creating a bond with the CO_2 molecule together with one of the oxygen atoms in the clay, and hence forming a CO_3 group. This is the only cation to form a CO_3 group in SCC-DFTB, and might be because it is both a small and divalent cation. Adding another CO_2 to Be-Fh breaks the CO_3, and adding the third CO_2, beryllium is brought back into the cavity. Another interesting observation is that it looks like beryllium bonds with one fluorine atom when it resides in the hexagonal cavity. The bond length $d_{\text{Be-F}} = 1.44$ Å, which is close to the bond length in BeF_2 of 1.34 Å. However, beryllium is not suitable for storing CO_2 in clay because of its poisonous nature.

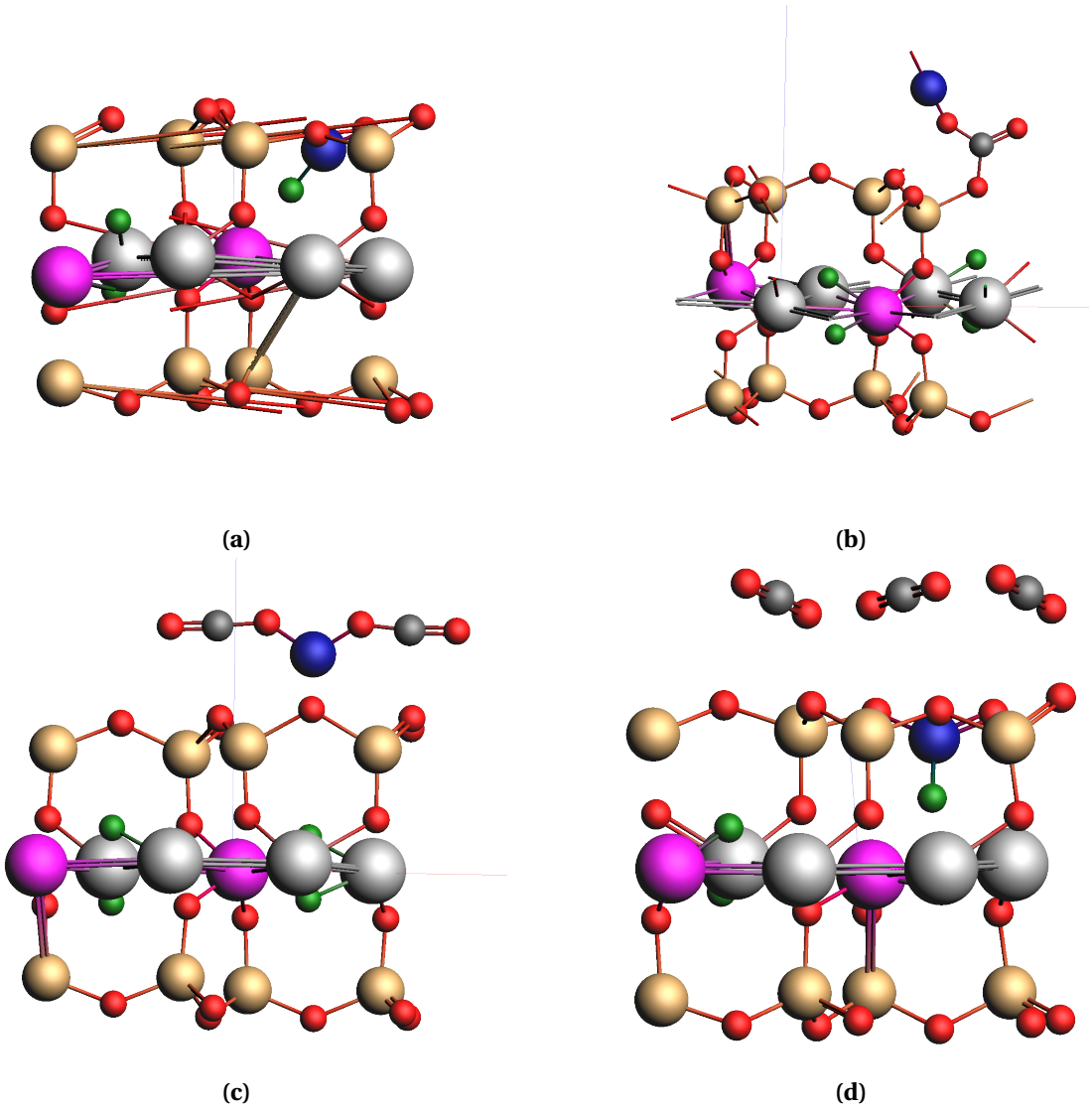

Figure 4.10: Geometry (SCC-DFTB) of the unit cell of fluorohectorite with Be as the interlayer cation for (a) plain Be-Fh, (b) Be-Fh with 1 CO_2, (c) Be-Fh with 2 CO_2, and (d) Be-Fh with 3 CO_2. (Mg = gray; F = green; O = red; Si = gold; Li = purple; C = black; X = blue.)

The reaction energy for Be-Fh and Mg-Fh is similar to K-Fh and Na-Fh with the same trend of increasing when adding 2 CO_2 and decreasing for the third CO_2. The increase in energy for both must be caused by the change in geometry. For Be-Fh this means breaking apart the CO_3 group, and for Mg-Fh magnesium "pops" back into the cavity. Both beryllium and magnesium are small cations and reside inside the cavity for 0 and 3 CO_2. For both, $d_{X–O}$ increase a lot going from 1 CO_2 to 2 CO_2.

Looking at d_{001} for Be-Fh in Figure 4.9b, it has a different trend than for Mg-Fh and Ca-Fh. It decreases when adding the first and second CO_2. Comparing this with the discussion for the geometry, the smaller values for d_{001} can be

understood in terms of the beryllium cation residing well above the hexagonal cavity. This might mean that the positively charged cation attracts the negatively charged bottom sheet of the oxygen layer above, and hence the decrease of d_{001}.

An interesting observation for the basal interlayer distance, also observed when comparing Li-Fh vs. K-Fh and Na-Fh, is how it for Ca-Fh with no CO_2 is so much smaller than Be-Fh and Mg-Fh. This despite magnesium and beryllium being smaller cations and position inside the hexagonal cavity. As discussed for Be-Fh when beryllium is positioned above the hexagonal cavity, here the positively charged calcium might attract the bottom sheet of the layer above it, and hence pull the layers together.

A difference for the divalent cations in group II compared to the cations in group I is that the octahedral sheet with magnesium and lithium is a little crooked. This is illustrated in the geometry for Be-Fh in Figures 4.10a and 4.10d when beryllium is positioned inside the hexagonal cavity. This might just be the charge of the cation that pulls the octahedral sheet in different directions.

4.2.2 GFN1-xTB

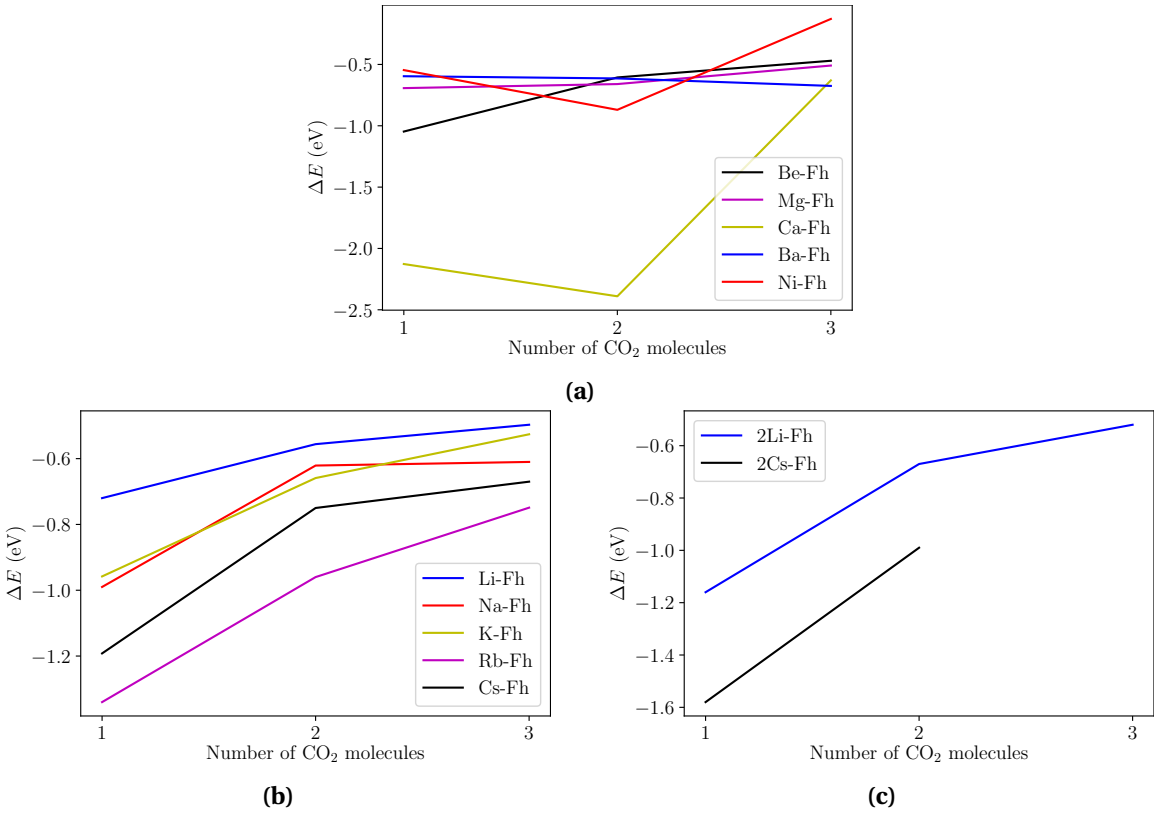

Figure 4.11: Reaction energies (GFN1-xTB) with 1, 2 and 3 intercalating CO_2 molecules and the different interlayer cations. (a) Group II cations, (b) one cation from group I and (c) two group I cations. 2Cs-Fh calculations failed for 3 CO_2.

With GFN1-xTB, only slab calculations were performed, since bulk calculations did not work properly with this method. It is interesting to see if any trends emerge, especially looking at larger interlayer cations like Rb^+, Cs^+, Ba^{2+} and Ni^{2+}. Especially Ni^{2+} has given good results in experiments [50].

The most interesting result from GFN1-xTB after looking at SCC-DFTB, is that the first CO_2 added to the various X-Fh formes CO_3 with one of the oxygens in fluorohectorite, and stays a CO_3 when adding more CO_2. X-Fh are illustrated in Figure 4.12. Another difference is that all the geometries for X-Fh are a lot more similar to each other than for geometries with SCC-DFTB. For example, all cations are positioned in the hexagonal cavity and not so much above the cavity, as some of the larger cations experienced for SCC-DFTB. This difference might be from the fact that GFN1-xTB computations are slab computations and not bulk as for SCC-DFTB.

There are some exceptions to these trends. Firstly, nickel and barium do not form CO_3 when adding the first CO_2, it is just a normal CO_2. For nickel, CO_3

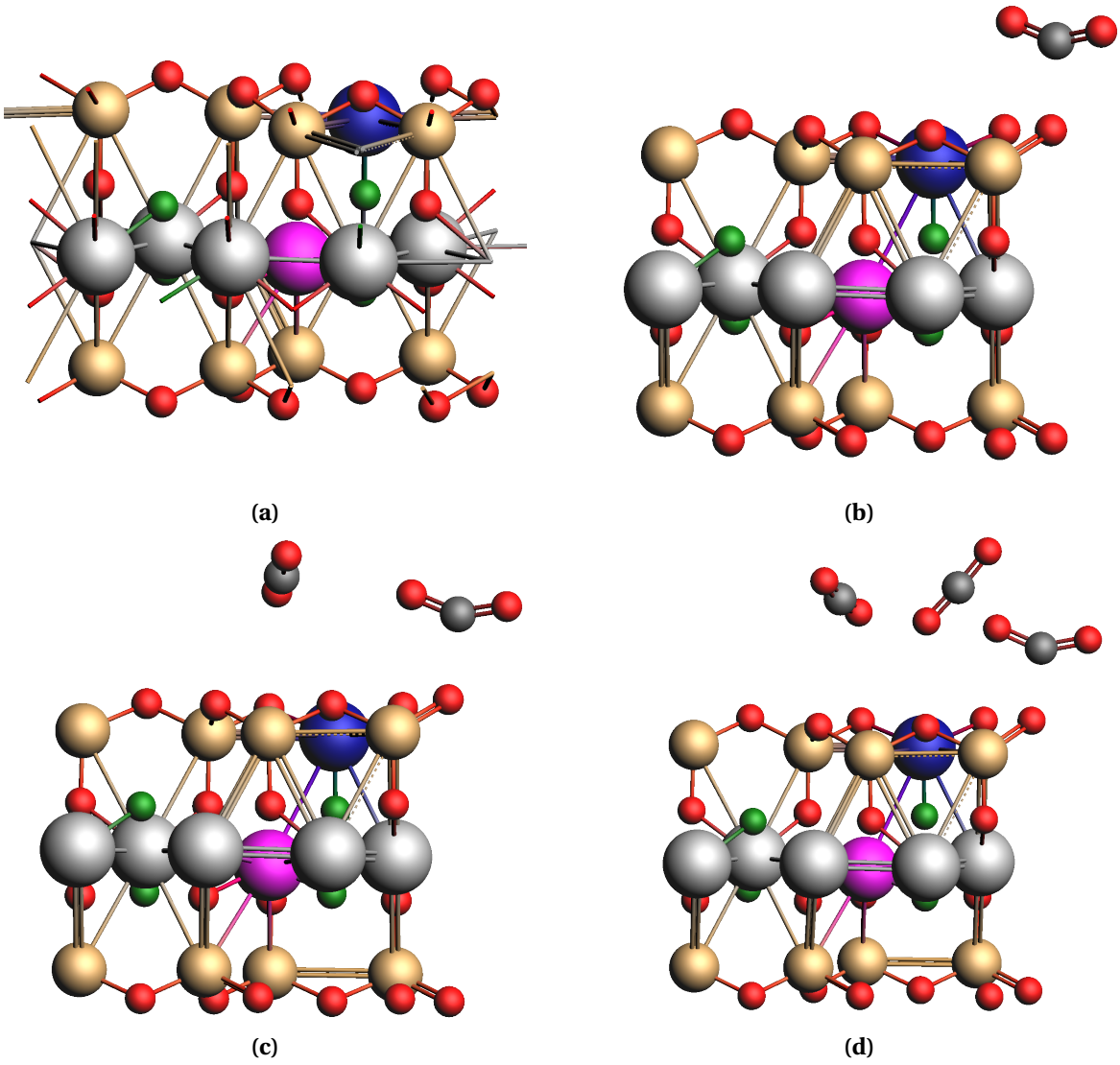

Figure 4.12: Geometry (GFN1-xTB) of the unit cell of fluorohectorite for (a) plain X-Fh, (b) X-Fh with 1 CO_2, (c) X-Fh with 2CO_2, and (d) X-Fh with 3 CO_2. (Mg = gray; F = green; O = red; Si = gold; Li = purple; C = black; X = blue.)

appears when adding more CO_2, and for barium CO_3 is formed when the third CO_2 is added. Secondly, for calcium with 2 CO_2, the first CO_2 is a CO_3, and the second CO_2 is not linear, but bent. Thirdly, the two divalent cations calcium and barium give a crooked geometry for the six cations in the octahedral sheet in the middle of the clay structure, illustrated in Figure 4.13. This probably comes from them being too large to fit properly into the cavity and hence pushing the other atoms away. Cesium is also a large cation, but it does not make the octahedral sheet crooked. Fouthly, both nickel and beryllium make a bond to one of the fluorine atoms in the clay material. The bond lengths are $d_{\text{Ni-F}} = 2.00$ Å and $d_{\text{Be-F}} = 1.59$ Å, which is not too different from the bond lengths in NiF_2 and BeF_2, which are $d_{\text{Ni-F}} = 1.64$ Å and $d_{\text{Be-F}} = 1.38$

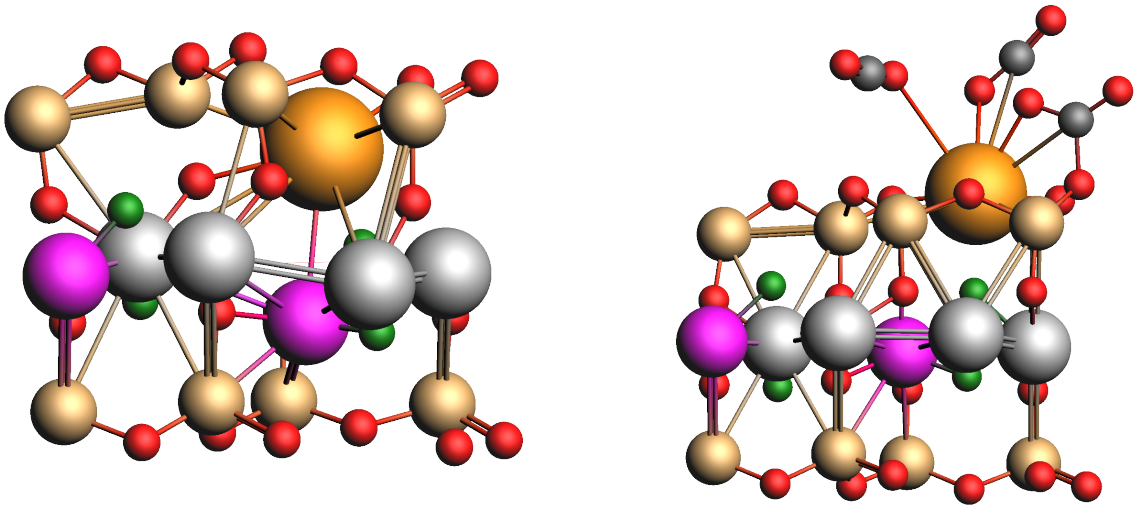

(a) **(b)**

Figure 4.13: Geometry (GFN1-xTB) of the unit cell of fluorohectorite with a cation as the interlayer cation for (a) Ba-Fh and Ca-Fh (essentially indistinguishable geometries), and (b) Ba-Fh and Cs-Fh with 3 CO_2 (essentially indistinguishable geometries). (Mg = gray; F = green; O = red; Si = gold; Li = purple; C = black; X = yellow.)

Å, respectively. Lastly, the CO_2 are mostly in the vacuum layer for all cations, parallel to the clay, but not for the large cations cesium, rubidium and barium. For Ba-Fh, Rb-Fh and Cs-Fh, the third CO_2 is positioned with more of an angle to the clay layer.

Looking at the reaction energies for group I cations in Figures 4.11b and 4.11c, the curves look the same as when looking at single cations and CO_2 without fluorohectorite, see Figure 4.2. That is, the reaction energy is large for adding 1 CO_2 into the clay, and then adding more CO_2 is less efficient. For SCC-DFTB the same trend arises for Li-Fh. The common denominator for SCC-DFTB Li-Fh and the monovalent cations with GFN1-xTB, is that the cation resides in the hexagonal cavity, which might be a reason for the reaction energy trend. However, there is no d_{001} to compare for GFN1-xTB. Also for group I cations, the energy increases with increasing cation size, apart from rubidium and cesium switching place, seen in Figure 4.11b.

Loganathan et al. found that calcium, magnesium and sodium need H_2O to prop the layer in clay open and thus adsorb CO_2 [54]. From this is interesting that Ca-Fh does so well energetically, seen in Figure 4.11a. It even binds more strongly with CO_2 than all group I cations. Nickel was expected to do especially well from experiments, however it does not stand out much from the other divalent cations. This might have been different with bulk computations. An interesting observation however, is that the trend in the reac-

# CO_2	Li-Fh	2Li-Fh	Na-Fh	K-Fh	Rb-Fh	Cs-Fh	2Cs-Fh	Be-Fh	Mg-Fh	Ca-Fh	Ba-Fh	Ni-Fh
1	-0.72	-1.17	-0.99	-0.96	-1.34	-1.19	-1.58	-1.05	-0.69	-2.13	-0.60	-0.55
2	-0.56	-0.67	-0.62	-0.66	-0.96	-0.88	-0.99	-0.61	-0.66	-2.39	-0.61	-0.87
3	-0.50	-0.52	-0.61	-0.53	-0.75	-0.67	-	-0.47	-0.51	-0.63	-0.67	-0.13

Table 4.6: Reaction energy ΔE (eV) for adsorption of the first three CO_2 molecules with one and two cations pr unit cell. (GFN1-xTB.) Cs-Fh calculations failed for 3 CO_2.

# CO_2	Li-Fh	2Li-Fh	Na-Fh	K-Fh	Rb-Fh	Cs-Fh	2Cs-Fh	Be-Fh	Mg-Fh	Ca-Fh	Ba-Fh	Ni-Fh
1	-	-	-	-	-	-	-	-	-	-	4.24	2.81
2	3.52	3.49	3.64	2.76	3.56	3.23	3.13	3.23	3.01	4.97	4.62	2.52
3	3.61	3.81	3.33	3.27	3.01	3.01	-	3.59	3.33	4.49	3.07	2.97

Table 4.7: Bond distances $d_{X–O}$ (Å) with upto three absorbed CO_2 molecules with one and two cations pr unit cell. (GFN1-xTB.)

# CO_2	Li-Fh	2Li-Fh	Na-Fh	K-Fh	Rb-Fh	Cs-Fh	2Cs-Fh	Be-Fh	Mg-Fh	Ca-Fh	Ba-Fh	Ni-Fh
1	1.93	1.72	1.80	1.77	1.73	1.73	1.63	1.73	1.93	1.52	-	-
2	1.93	1.71	1.77	1.75	1.69	1.70	1.58	1.73	1.87	1.41	-	1.80
3	1.81	1.67	1.69	1.67	1.66	1.64	-	1.70	1.72	1.41	1.46	1.72

Table 4.8: Average C–O bond distance $d_{C–O}$ (Å) in the CO_3 group with various CO_2 done with GFN1-xTB.

tion energy for divalent cations is different from group I cations. Instead of decreasing with increasing amounts of CO_2, the form of the graph is more similar to the reaction energy for many structures done with SCC-DFTB, a v-shaped curve.

Looking at Table 4.7 for the X–O distance between the CO_2 and the cations, the trend is an increased $d_{X–O}$ for increasing amounts of CO_2, which was also the case for some SCC-DFTB computations, especially for the last CO_2 added. The C–O distance between an oxygen in the clay layer and the carbon in the CO_3 formation in general decreases for increasing amounts of CO_2 added to the system, which is the opposite for $d_{X–O}$. This can be seen in Table 4.8. The shortest $d_{C–O}$ is for Ca-Fh with 3 CO_2. With $d_{C–O}$ = 1.41 Å, it is close to the distance for a C–O bond in CO_3, which is 1.31 Å. These bonds are more symmetric than for the other structures and close to a real CO_3 structure. For 2Cs-Fh with 3 CO_2 there are no results. This is because the geometry could not be optimized with GFN1-xTB. It was not possible to do computations for 2Na-Fh, 2K-Fh and 2Rb-Fh because the AMS program crashed [2]. However, being able to do the same computations for 2Li-Fh might be because lithium is small enough to "hide" inside the hexagonal cavity.

However, comparing the results for 2Li-Fh and Li-Fh, the geometries are practically identical. The only difference is that there is a second cation for 2Li-Fh, mirroring the first cation, sitting in the bottom hexagonal cavity just as for the top cation. For both 2Li-Fh and Li-Fh, $d_{X–O}$ increases with increasing amounts of CO_2, while the $d_{C–O}$ decrease. The similarities between 2Li-Fh and Li-Fh also apply to 2Cs-Fh vs. Cs-Fh. It would not be very drastic to assume that this would apply also for the third CO_2 for 2Cs-Fh. The difference between one and two intercalated cations can be seen in the reaction energies. For two cations this energy is larger than for one cation.

In conclusion, the charge of the cation will influence the uptake of CO_2 in clay, as seen in experiments [50]. A cation will polarize the non-polar CO_2 molecule, which gives a larger interaction between the two. This seems to agree with the results from our simulations as well. Experiments have shown that the clay–cation interaction might be more important than the polarization between the cation and CO_2 [55]. This also seems to be the case in this thesis, as the differences between the various Fh structures are relatively

[2] Information from SCM said that the GFN1-xTB model collapses for periodic systems where the bonding situation is "molecule like", like organic crystals. This comes from a problem with the original parametrization not supporting materials and periodic systems.

small.

4.3 Vibrational Frequencies

CO_2 is a linear molecule, and the expected outcome of adding a cation to CO_2 is a linear molecule with a X–O–C angle of approximately 180°. This is the case for most cations, see Figure 4.14a. However, the Ni–O–C angle is 152.2° with revPBE, and 172.5° with GFN1-xTB, illustrated in Figure 4.14b. With GFN1-xTB, the Mg–O–C angle is also less than 180°, at 157.8°. With SCC-DFTB the two cations calcium and sodium have a bent angle, with a Ca–O–C=156.5° and a Na–O–C=164.5°. These cations with non-linear geometry will hence give an extra vibrational frequency, which is a non-degenerate bending mode. Vibrational frequencies are typically given in units of cm^{-1}.

The selection of what cations give rise to a bend in the geometry seems arbitrary. Some are divalent, some are large cations, and there is no trend. If the modes were not bent, the trend would be that the larger the cation, the larger frequency for the bending mode.

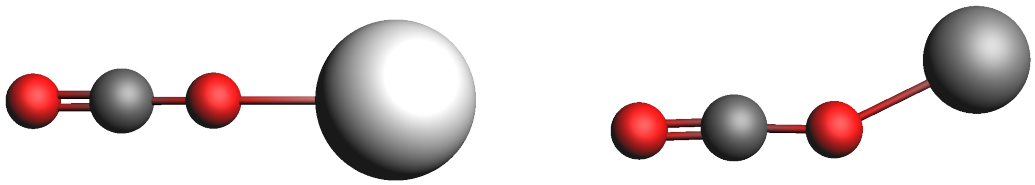

(a) **(b)**

Figure 4.14: The two geometries of a cation and 1 CO_2. (a) Most cations give a linear geometry, (b) some give a non-linear geometry. The latter apply to Ni^{2+} (revPBE), Mg^{2+} and Ni^{2+} (GFN1-xTB), and Ca^{2+} and Na^{+} (SCC-DFTB). (O = red; C = black; X = gray.)

Figure 4.15 and Table 4.9 compare the various vibrational modes for a single molecule of CO_2, without the cations, for the three calculation methods revPBE, SCC-DFTB and GFN1-xTB, and the experimental values from National Institute of Standards and Technology (NIST) [56]. The three methods

Vibrational frequency	revPBE	SCC-DFTB	GFN1-xTB	Experimental
Asymmetric stretch	2338	2929	2612	2349
Symmetric stretch	1292	1614	1447	1333
Bending mode	449	549	628	667

Table 4.9: Comparing the vibrational frequencies (cm^{-1}) for CO_2 with the three different computation models and experimental values [56].

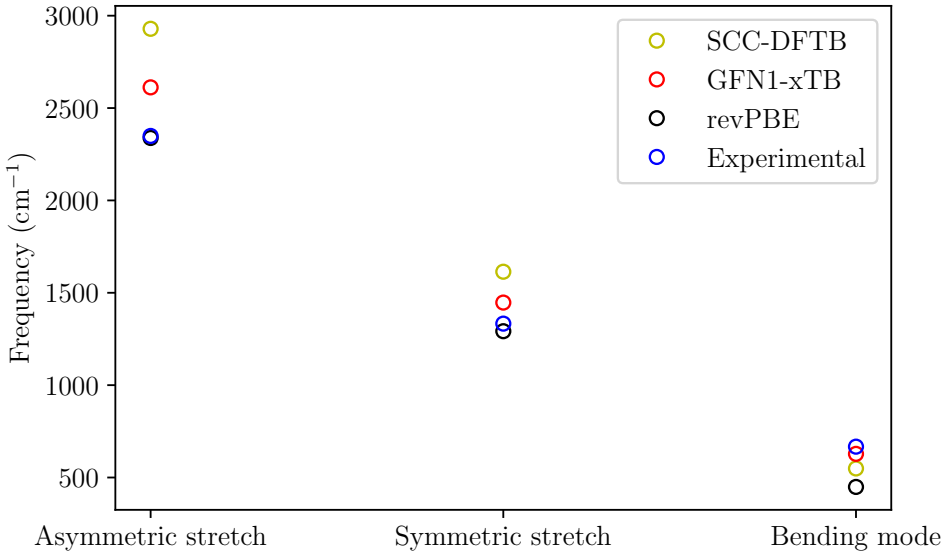

Figure 4.15: Comparing the vibrational frequencies for CO_2 with the three different computation models and experimental values [56].

give rather large differences in the vibrational frequencies. For the asymmetric stretch, GFN1-xTB yields ca. 300 cm^{-1} larger than revPBE, and SCC-DFTB is ca. 300 cm^{-1} larger than GFN1-xTB. The symmetric stretch deviates only 200 cm^{-1} between the three methods. For both stretching modes, the revPBE method is closest to experimental results from NIST, which are 2349 cm^{-1} for the asymmetric stretch and 1333 cm^{-1} for the symmetric stretch [56]. SCC-DFTB is the method furthest away from the experimental values. However, for the bending mode, SCC-DFTB is closer to the experimental values, and revPBE is furthest away. This difference is not as large as for the asymmetric and symmetric stretch.

These differences between the three methods are also observed when adding various cations to CO_2 and calculating the vibrational frequencies. The vibrational frequencies computed with SCC-DFTB and GFN1-xTB are in general larger than for revPBE.

In Figure 4.16, all three modes are illustrated from revPBE calculations. The

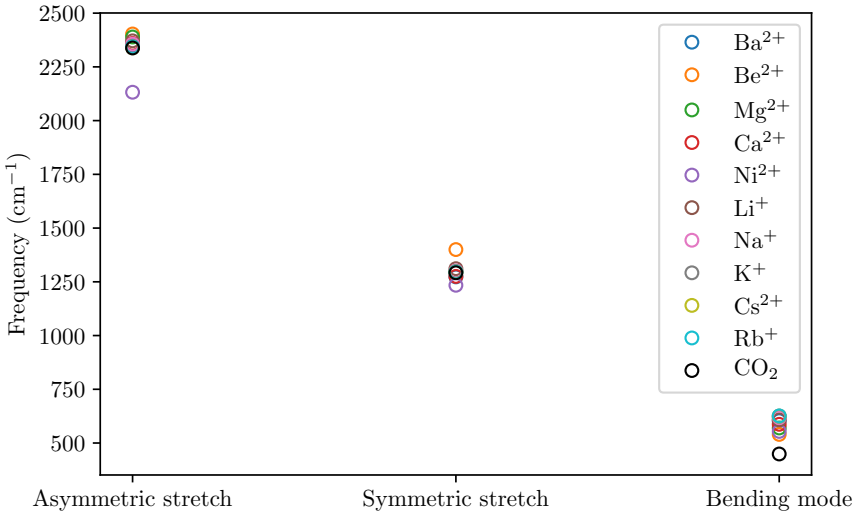

Figure 4.16: The revPBE vibrational frequencies for CO_2 when a single CO_2 is put together with a cation from group I and II as well as nickel.

asymmetric stretch lies in the range 2100–2400 cm^{-1}, the symmetric stretch around 1200–1400 cm^{-1} and the bending modes lie around 600 cm^{-1}. For the asymmetric and symmetric stretch, nickel stands out. The value for nickel is considerably smaller than with other cations. This might be explained by it being a transition metal. Hence it is very different from the other cations. Beryllium also stands out for the asymmetric and symmetric stretch, having the largest frequencies for both stretches.

Results for the asymmetric and symmetric stretch for the different computation methods are illustrated in more detail in Figures 4.17 and 4.18, respectively. The frequencies decrease when the mass of the cation increases within a group. This is understandable in terms of a simple one-dimensional harmonic oscillator. The vibration frequency depends on a mass and a spring constant, $f = \omega/2\pi = \sqrt{k/m}/2\pi$ [57, p. 412]. In a system with several atoms and hence several masses and spring constants, these are seen as an "effective mass" and "effective spring constant".

For the symmetric modes, the cation vibrates in phase with the oxygen furthest away, and out of phase with the closest oxygen. Hence the harmonic oscillator approach seems reasonable. For the asymmetric modes the cation is essentially at rest and therefore the mass of the cation is not the reason for the trend we see in the vibrational frequencies. However, the bond between the atoms might decrease with increasing mass and hence give rise to these results. Another interesting observation is that the symmetric stretch is IR active for CO_2 together with a cation, while it is IR inactive for CO_2 alone.

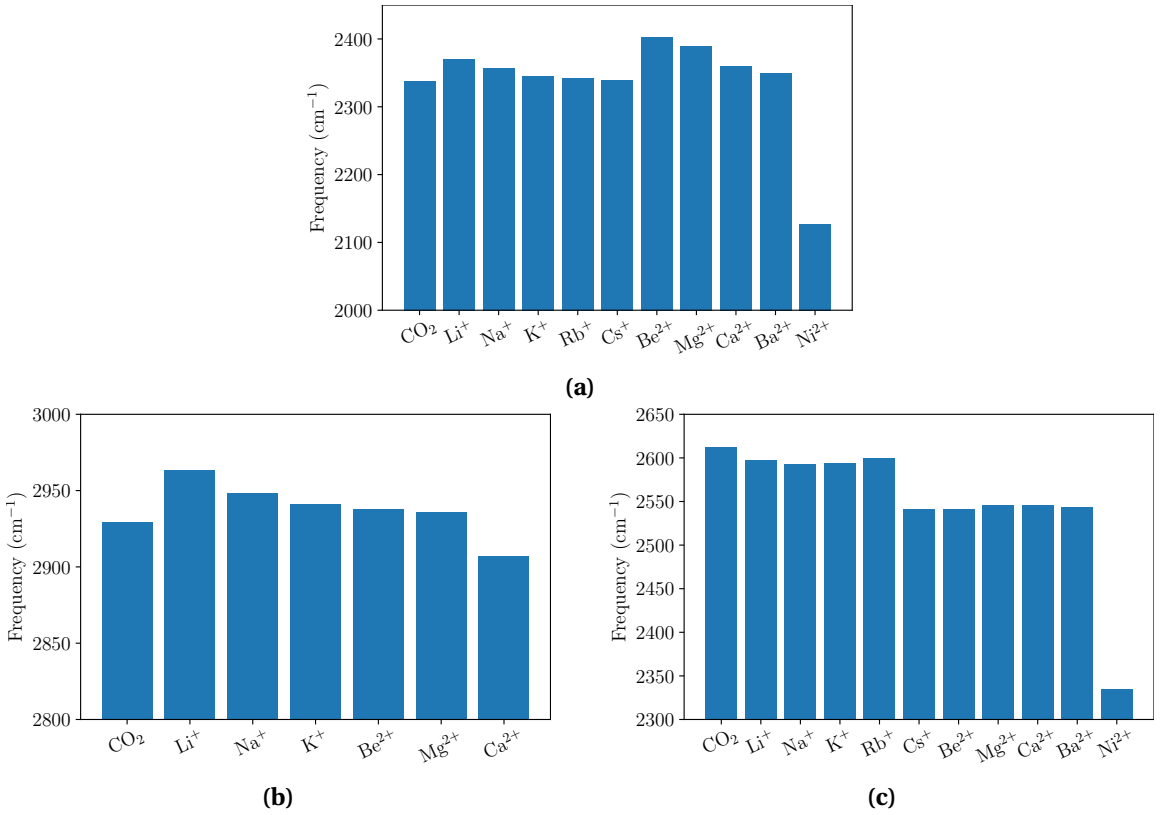

Figure 4.17: Asymmetric stretch for CO_2 when put together with the various cations, compared to the vibrational modes for CO_2 alone. (a) revPBE, (b) SCC-DFTB and (c) GFN1-xTB.

As mentioned earlier, some of the cations give rise to a non-linear geometry with SSC-DFTB and GFN1-xTB. The cations with non-linear geometries breaks the trend for decreasing frequency for increasing mass. In Figure 4.18b, sodium should be larger for the trend to fit properly. This holds group II magnesium in Figure 4.18c as well. Also breaking the trend is the group I elements in GFN1-xTB, where the frequencies has a slight increase for increasing mass.

From computations with revPBE, the trend of the bending modes are increased frequencies with increased mass, see Figure 4.19a. In general, SCC-DFTB and GFN1-xTB does not match the trend from revPBE. This might partly be because of the non-linear geometry that gives rise to to non-degenerate bending modes. These non-degenerate modes can be seen in Figure 4.19 and are marked in gray. Also standing out are the bending modes for group I for GFN1-xTB in Figure 4.19c which seem to converge to 624 cm^{-1}. If the spring constant does not change, there should be an asymmetric boundary value for increasing mass, which 624 cm^{-1} seems to be in this case. Another interesting observation is that beryllium gives rise to a non-degenerate bending mode even though the geometry is linear with a Be–O–C angle of 180°.

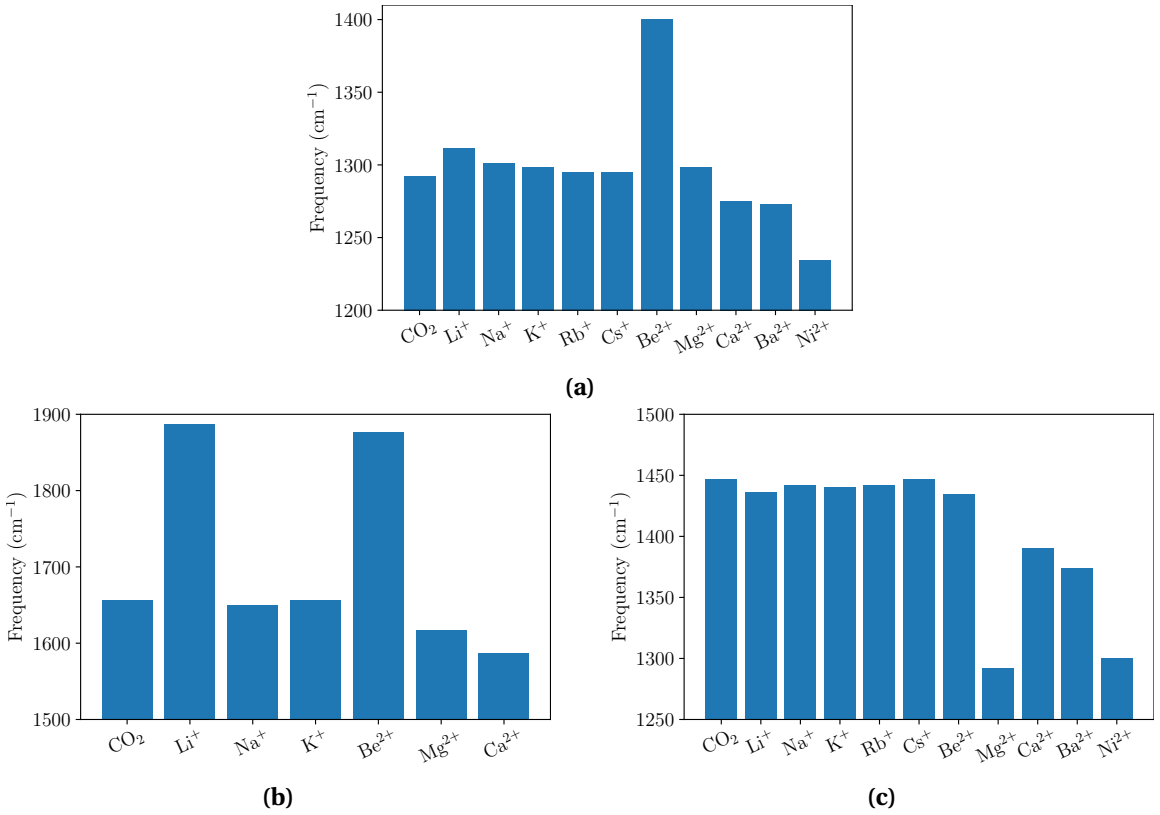

Figure 4.18: Symmetric stretch for CO_2 when put together with the various cations, compared to the vibrational modes for CO_2 alone. (a) revPBE, (b) SCC-DFTB and (c) GFN1-xTB.

The nonlinear geometries, and hence non-degenerate bending modes, from computations with GFN1-xTB and SCC-DFTB is different than for revPBE. This might be explained by the models themselves. The second derivatives in the Hessian matrix might not be correct and hence give too large values.

Compared to the experimental result from NIST, which gives a frequency of 667 $^{-1}$ for the bending mode for a single CO_2 [56], the revPBE bending modes are the closest. The bending modes for SCC-DFTB are too small and GFN1-xTB are a little too large, which is surprising from comparing methods for a single CO_2 in Figure 4.15.

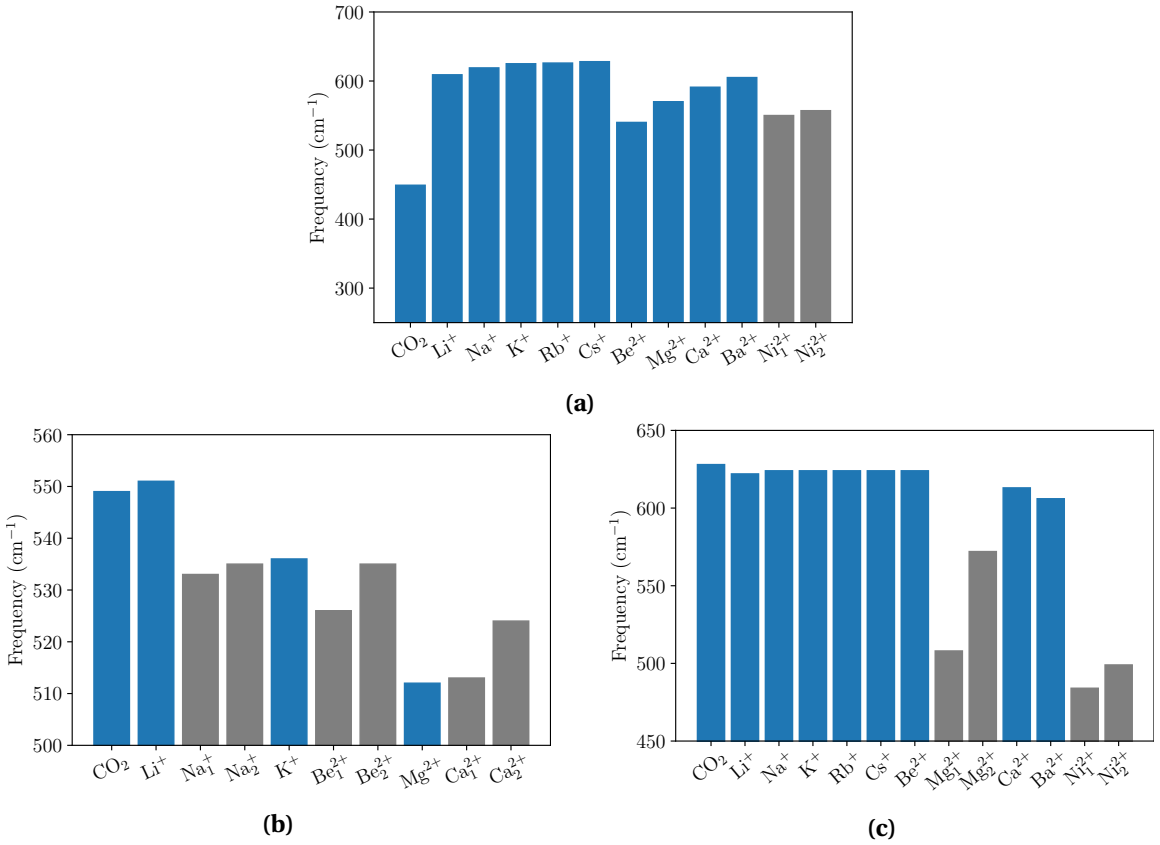

Figure 4.19: Bending modes for CO_2 when put together with the various cations, compared to the vibrational modes for CO_2 alone. (a) revPBE, (b) SCC-DFTB and (c) GFN1-xTB. Blue bars are the degenerate modes from linear molecules, and gray bars for non degenerate modes from non-linear molecules.

Cations in Fluorohectorite

CO_2 in Fh vibrates together with the atoms of Fh. The frequencies for the bending modes of CO_2 are very close to many of the frequencies of the atoms in Fh. This coupling makes it difficult to distinguish the bending modes of CO_2 from the other frequencies. For this reason, the bending modes will not be discussed any further. However, the large values for the asymmetric and symmetric stretch modes for CO_2 are easier to observe. Vibrational frequency computations for revPBE are not within the scope of this thesis, and the coming discussion of vibrational frequencies will be for SCC-DFTB (3D bulk systems) and GFN1-xTB (2D slab systems). Only systems with one adsorbed CO_2 molecule will be discussed, to avoid the complexity of multiple vibrational modes when two or more CO_2 molecules are present.

In Figure 4.20, a summary of the asymmetric CO_2 stretch frequency is presented for bulk systems (4.20a; SCC-DFTB) and slab systems (4.20b; GFN1-xTB). Figure 4.21 gives a similar summary of the symmetric CO_2 stretch fre-

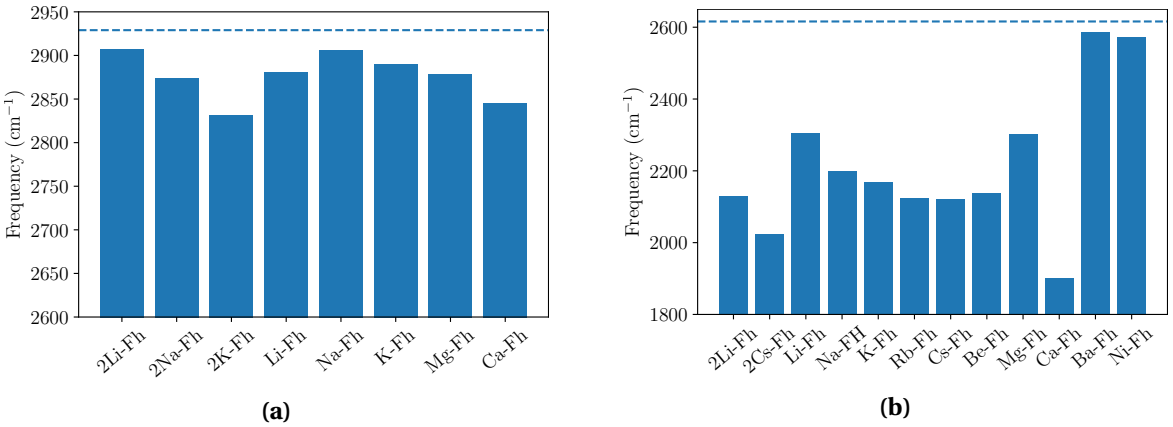

Figure 4.20: Asymmetric stretch for 1 CO_2 in Fh for (a) SCC-DFTB and (b) GFN1-xTB. The dashed line represents the asymmetric stretch for CO_2 in the respective models. (For SCC-DFTB, Be-Fh is an outlier of 2125 cm^{-1} and not in the plot.)

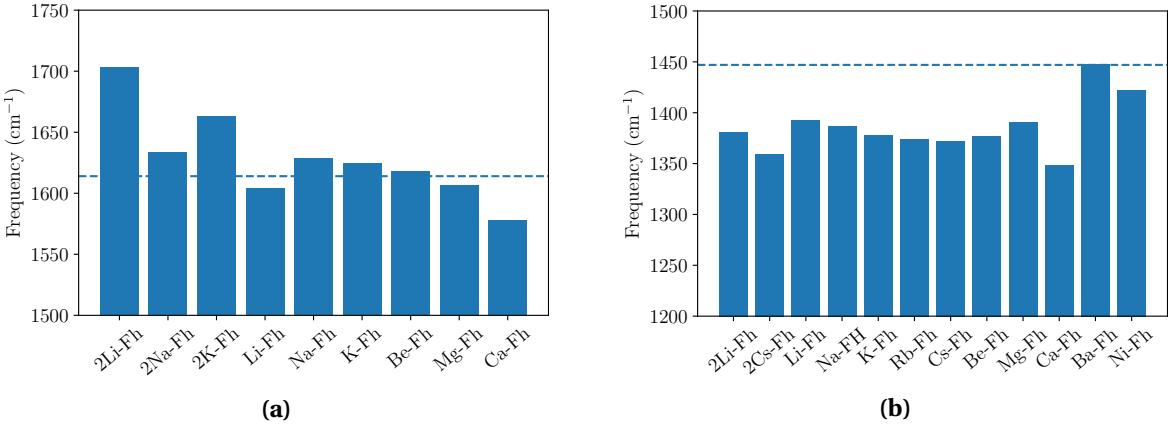

Figure 4.21: Symmetric stretch for 1 CO_2 in Fh and various cations, for (a) SCC-DFTB and (b) GFN1-xTB. The dashed line represents the symmetric stretch for CO_2 in the respective models.

quency. For both models, the asymmetric stretch frequencies for CO_2 in Fh are smaller than for a single CO_2. The symmetric stretch frequencies with GFN1-xTB are also smaller than for a single CO_2, except for Ba-Fh, which is approximately unchanged. For symmetric stretch frequencies with SCC-DFTB, 2Li-Fh and 2K-Fh give a large increase, 2Na-Fh, Na-Fh, K-Fh and Be-Fh are close to the frequency of the single CO_2, while the rest of the structures have smaller frequencies than a single CO_2.

For Ni-Fh, there is only a small reduction in both asymmetric and symmetric stretch. This is consistent with the geometry. There is a relatively weak bond between nickel and CO_2 because of the relatively long X–O distance of $d_{X–O}$ = 2.82 Å. The frequencies are only moderately affected by the environment of CO_2.

The asymmetric stretch for Be-Fh is an outlier in the SCC-DFTB system, with

a small value compared to the other structures, and is hence not in the plot of Figure 4.20a. The other structures have a frequency around 2850 cm^{-1}, while it in Be-Fh is 2125 cm^{-1}. As illustrated in Figure 4.10b, the geometry of Be-Fh is special because of the relatively symmetric CO_3 group. Beryllium forms a connection between one oxygen atom in CO_2 and an oxygen atom in the clay layer above. The asymmetric stretch for CO_3 in SCC-DFTB is 1595 cm^{-1}, which beryllium is closer to than the single CO_2 frequency of 2929 cm^{-1}. The Be-Fh symmetric stretch at 1618 cm^{-1} is also close to one of the symmetric stretches in CO_3 of 1594 cm^{-1}.

Looking at the asymmetric vibrations for SCC-DFTB, Figure 4.20a, the frequencies for two group I cations decrease with increasing mass. Within one group I cations, the frequency overall increase with increasing mass of the cation, while it decrease with mass for the divalent cations. However, K-Fh gives a slightly smaller frequency than for Na-Fh, and as already mentioned, Be-Fh is a large deviation. For two cations and the divalent cations, this trend coincides with the trends seen for the asymmetric modes for SCC-DFTB without Fh, but the values are ca. 100 cm^{-1} smaller when in Fh. In summary, the movement of CO_2 decreases when it is inserted into X-Fh due to its interaction with the other atoms in the clay.

Looking at Figure 4.20b, the asymmetric stretch frequencies vary more for GFN1-xTB than for SCC-DFTB, from 1900 cm^{-1} for Ca-Fh to 2587 cm^{-1} for Ba-Fh. The values are in general smaller than for SCC-DFTB. The large span in frequencies is quite striking based on how similar the geometries for GFN1-xTB were, discussed in Section 4.2.2. Two cations in Fh give decreasing frequencies for increasing mass, as for SCC-DFTB. This trend also applies for the other group I cations. However, the frequencies for the divalent cations generally increase with increasing mass. Here, Ca-Fh stands out with its small value and not following the trend for its group. Compared to the frequencies for CO_2 and cations without Fh, the frequencies are smaller by ca. 200 cm^{-1} for group I cations, while the difference is not very large for the largest divalent cations.

A surprising result looking at the values for the GFN1-xTB asymmetric stretch, is that some of them seem be too large for CO_3 groups. The asymmetric stretch for CO_3 with GFN1-xTB 1385 cm^{-1}. From looking at the geometries in Figure 4.12, most of the geometries gave the formation of CO_3. An explanation for this might be that even though from the geometry it looks like a CO_3 has formed, the CO_2 and the oxygen below might not be as strongly bonded

as it looks like. The CO_2 is still intact, but with a bent geometry. Ca-Fh and 2Cs-Fh have small enough frequencies to be very close to CO_3.

The frequencies can also be seen in connection to the C–O distances, (Table 4.8). Ca-Fh has the shortest distance to the oxygen below, and can be another indication that this bond actually is CO_3. The second shortest distance is for 2Cs-Fh, which also supports this idea because of the small stretch frequencies. The large frequencies for Ba-Fh and Ni-Fh can be explained by the discussion from Section 4.2.2. For both these geometries, there is no CO_3, but plain CO_2, which gives larger frequencies.

The general trend for the symmetric stretch frequencies in SCC-DFTB, see Figure 4.21a, is a decreasing frequency for increasing mass within a group. This does not apply to Li-Fh and 2Na-Fh, which have lower values. These also have a larger distance between the cation and the CO_2 within their group, from Table 4.4. However, Be-Fh does not deviate from the trend as it did for the asymmetric modes. This might be due to the CO_3 bond not influencing the symmetric modes. This missing deviation of Be-Fh can be a little surprising from the results from the cation and CO_2 without Fh in Figure 4.17b. For the four atom system, the symmetric vibration for Be is a lot larger than for the other atoms. However, in the Fh structure, there are many atoms and bonds that can be the reason for this.

For the symmetric vibrations for GFN1-xTB, seen in Figure 4.21b, the trend is the same as for the asymmetric vibrations for the same model. Within groups, the vibrations decrease with increasing mass. As for the asymmetric modes, Ba-Fh and Ni-Fh do not follow the trend, and are larger than for the other molecules. This because there is no CO_3. Also, the frequency for Ca-Fh is here smaller than for the other structures, as for the asymmetric mode. Again, for Ca-Fh the CO_2 molecule has a shorter distance to the other oxygen atom forming CO_3 with than the other structures.

The general trend for the frequencies when adding more CO_2 is that the frequency belonging to CO_3 decreases for each CO_2 added. This also adds up when the distance decreases, meaning the CO_2 bond is weakened.

In conclusion, the vibrational frequencies supports the idea that CO_3 is formed for all structures in GFN1-xTB computations except for Ni-Fh and Ba-Fh, and only for Be-Fh with SCC-DFTB. Also, the structures with the shortest $d_{C–O}$ seem to be the structures with the lowest frequencies and hence strongest CO_3 bonds.

Chapter 5

Conclusion

5.1 Concluding Remarks

A DFT and DFTB study was conducted to see how different cations would bind to CO_2 in fluorohectorite, in an attempt to predict whether they can be used in fluorohectorite for CO_2 storage.

SCC-DFTB is seen as a better method to model clay molecules than GFN1-xTB. This because it can model a 3D molecule, which is not the case for GFN1-xTB. 3D computations take swelling into account, which is a physical component important for clay materials. The parametrization for DFTB has a geometry focus and hence the reaction energies are given low priority.

The trends show that for SCC-DFTB the reaction energy is the most optimal when adding 2 CO_2 and that the interlayer distance increases with an increasing amount of CO_2. This means more swelling and is in accordance with experimental results [50]. The systems with two intercalated cations per unit cell do not lead to more swelling than for one cation. They also require more energy to get 1 CO_2 into fluorohectorite, but they will give better reaction energies for larger amounts of CO_2. For one group I cation, CO_2 is more tightly bound with the cation for larger cations.

Common to both models is that the reaction energies in general seem to increase when the cation is residing in the interlayer, above the hexagonal cavity. This is possible when when the intercalated cation is too large to reside inside the cavity. For the positioning for CO_2, it seems like they prefer to be parallel to the clay surface.

For GFN1-xTB, the results show that the reaction energy decreases when adding

more CO_2 to the Fh structures. At the same time, the cation–oxygen bond length increases. Ca-Fh performed the best, with $\Delta E = -2.39$ eV for 2 CO_2. The tendency is that larger cations bind CO_2 better, and cations with valence of two have higher reaction energies than cations with valence of one. This can be seen from the larger reaction energies and the smaller X–O distances. This might also be the case when larger atoms can be tested with SCC-DFTB in the future when it supports larger atoms in its parametrization.

All GFN1-xTB computations give a geometry which looks like a CO_3 group. The vibrational frequency analysis can help understanding these geometries. Very small frequencies means a more likeliness for a structure with CO_3, especially seen in the context of a short C–O distance. This applies to Ca-Fh and 2Cs-Fh. Ba-Fh and Ni-Fh have large frequencies, which means non-existing CO_3 groups. With increased amounts of CO_2, the C–O distance decreases, which means a weakening of the CO_2 bond.

5.2 Further Studies

Future work should include computations on systems of fluorohectorite with CO_2 and H_2O, as water helps the clay prop open and accommodate more CO_2 [54, 5]. Looking at the atomic density profiles might also give a better understanding of where the various atoms could be placed. The start geometry could also be changed and hence give different results with more stable geometries.

Some studies show that it is possible to get more amounts of intercalated CO_2 for every cation, especially for cations like nickel [50]. It would be interesting to see if the trends found in this thesis would be replicated also for more amounts of intercalated CO_2.

When the parametrization of SCC-DFTB in the future supports larger atoms than calcium, it would be of interest to do bulk computations with these larger atoms as intercalated cations, especially nickel. If the computations capacity is present, these kind of computations could be done with revPBE. Another possibility is to use a different program than AMS which might support larger atoms, and hence make it possible to look at the basal interlayer distance.

References

[1] IPCC. *Climate change 2001: The scientific basis. Contribution of Working Group I to the third assessment report of the Intergovernmental Panel on Climate Change*. Cambridge and New York: Cambridge University Press., 2001.

[2] IPCC. *Climate change 2013: The physical science basis. Contribution of Working Group I to the fifth assessment report of the Intergovernmental Panel on Climate Change*. Cambridge and New York: Cambridge University Press., 2013.

[3] S. J. Davis, N. S. Lewis, M. Shaner, S. Aggarwal, D. Arent, I. L. Azevedo, S. M. Benson, T. Bradley, J. Brouwer, Y.-M. Chiang, et al. Net-zero emissions energy systems. *Science*, 360(6396):eaas9793, 2018.

[4] J. Tollefson. The hard truths of climate change—by the numbers. *Nature*, 573:324–327, 2019.

[5] V. Romanov. *Greenhouse Gases and Clay Minerals: Enlightening Down-to-Earth Road Map to Basic Science of Clay-Greenhouse Gas Interfaces*. Springer International Publishing AG, 2018.

[6] K. S. Lackner, S. Brennan, J. M. Matter, A.-H. A. Park, A. Wright, and B. Van Der Zwaan. The urgency of the development of CO_2 capture from ambient air. *Proceedings of the National Academy of Sciences*, 109(33):13156–13162, 2012.

[7] S. Fuss, W. F. Lamb, M. W. Callaghan, J. Hilaire, F. Creutzig, T. Amann, T. Beringer, W. de Oliveira Garcia, J. Hartmann, T. Khanna, et al. Negative emissions—part 2: costs, potentials and side effects. *Environmental Research Letters*, 13(6):063002, 2018.

[8] Climework. Our technology. `http://www.climeworks.com/our-technology/`. (Accessed on 11/03/2019).

[9] D. S. Scholl, and J. A. Steckel. *Density Functional Theory: A practical introduction*. John Wiley and Sons Ltd, 2009.

[10] Climework. How we do it. `https://climeworks.shop/how-it-works/`. (Accessed on 11/03/2019).

[11] L. Michels, J. O. Fossum, Z. Rozynek, H. Hemmen, K. Rustenberg, P. A. Sobas, G. N. Kalantzopoulos, K. D. Knudsen, M. Janek, T. S. Plivelic, et al. Intercalation and retention of carbon dioxide in a smectite clay promoted by interlayer cations. *Scientific reports*, 5:8775, 2015.

[12] K. K. Seljelid. *CO_2 Capture and Storage in Fluorohectorite Clay. Role of Pressure, Temperature and Interlayer Cation: XRD Studies*. Master's thesis, NTNU, 2019.

[13] P. Hohenberg and W. Kohn. Inhomogeneous electron gas. *Physical review*, 136(3B):B864, 1964.

[14] W. Kohn and L. J. Sham. Self-consistent equations including exchange and correlation effects. *Physical review*, 140(4A):A1133, 1965.

[15] R. O. Jones. Density functional theory: its origins, rise to prominence, and future. *Reviews of modern physics*, 87(3):897, 2015.

[16] The Nobel Prize. The nobel prize in chemistry. https://www.nobelprize.org/prizes/chemistry/. (Accessed on 11/29/2019).

[17] P. Hofmann. *Solid State Physics: An Introduction*. Wiley-VCH Verlag GmbH & Co. KGaA., 2015.

[18] P. C. Hemmer. *Kvantemekanikk*. Tapir, 1993.

[19] B. Hammer, L. B. Hansen, and J. K. Nørskov. Improved adsorption energetics within density-functional theory using revised perdew-burke-ernzerhof functionals. *Physical Review B*, 59(11):7413, 1999.

[20] Y. Zhang and W. Yang. Comment on "generalized gradient approximation made simple". *Physical Review Letters*, 80(4):890, 1998.

[21] A. R. Leach and A. R. Leach. *Molecular modelling: principles and applications*. Pearson education, 2001.

[22] C. Fox. An introduction to the calculus o. *Variations*, 1950.

[23] SCM. Mode Selective analysis, howpublished=https://www.scm.com/doc/ams/tasks/vibrationalanalysis/mode_selective_analysis.html#modescanning.

[24] P. C. Hemmer. *Faste stoffers fysikk*. Tapir, 1987.

[25] J. R. Ferraro. *Introductory raman spectroscopy*. Elsevier, 2003.

[26] SCM. DFTB manual 2019.3. https://www.scm.com/doc/DFTB/index.html. (Accessed on 04/20/2020).

[27] J. Singleton. *Band theory and electronic properties of solids*, volume 2. Oxford University Press, 2001.

[28] A. F. Oliveira, G. Seifert, T. Heine, and H. A. Duarte. Density-functional based tight-binding: an approximate DFT method. *Journal of the Brazilian Chemical Society*, 20(7):1193–1205, 2009.

[29] M. Elstner, D. Porezag, G. Jungnickel, J. Elsner, M. Haugk, T. Frauenheim, S. Suhai, and G. Seifert. Self-consistent-charge density-functional tight-binding method for simulations of complex materials properties. *Physical Review B*, 58(11):7260, 1998.

[30] SCM. Model Hamiltonians, https://www.scm.com/doc/DFTB/DFTB_Model_Hamiltonian.html#slater-koster-based-dftb. (Accessed on 04/27/2020).

[31] SCM. K-Space, https://www.scm.com/doc/BAND/Accuracy_and_Efficiency/K-Space_Integration.html. (Accessed on 04/22/2020).

[32] SCM. K-Space, https://www.scm.com/doc/DFTB/DFTB_Model_Hamiltonian.html#k-space-integration. (Accessed on 04/22/2020).

[33] H. J. Monkhorst and J. D. Pack. Special points for brillouin-zone integrations. *Physical review B*, 13(12):5188, 1976.

[34] P. Pracht, E. Caldeweyher, S. Ehlert, and S. Grimme. A robust non-self-consistent tight-binding quantum chemistry method for large molecules, 2019.

[35] S. Grimme, J. Antony, S. Ehrlich, and H. Krieg. A consistent and accurate ab initio parametrization of density functional dispersion correction (DFT-D) for the 94 elements H-Pu. *The Journal of chemical physics*, 132(15):154104, 2010.

[36] E. J. Baerends, T. Ziegler, A. J. Atkins, J. Autschbach, O. Baseggio, D. Bashford, A. Bérces, F. M. Bickelhaupt, C. Bo, P. M. Boerrigter, L. Cavallo, C. Daul, D. P. Chong, D.V. Chulhai, L. Deng, R. M. Dickson, J. M. Dieterich, D. E. Ellis, M. van Faassen, L. Fan, T. H.

Fischer, C. Fonseca Guerra, M. Franchini, A. Ghysels, A. Giammona, S. J. A. van Gisbergen, A. Goez, A. W. Götz, J. A. Groeneveld, O. V. Gritsenko, M. Grüning, S. Gusarov, F. E. Harris, P. van den Hoek, Z. Hu, C. R. Jacob, H. Jacobsen, L. Jensen, L. Joubert, J. W. Kaminski, G. van Kessel, C. König, F. Kootstra, A. Kovalenko, M. V. Krykunov, E. van Lenthe, D. A. McCormack, A. Michalak, M. Mitoraj, S. M. Morton, J. Neugebauer, V. P. Nicu, L. Noodleman, V. P. Osinga, S. Patchkovskii, M. Pavanello, C. A. Peeples, P. H. T. Philipsen, D. Post, C. C. Pye, H. Ramanantoanina, P. Ramos, W. Ravenek, J. I. Rodríguez, P. Ros, R. Rüger, P. R. T. Schipper, D. Schlüns, H. van Schoot, G. Schreckenbach, J. S. Seldenthuis, M. Seth, J. G. Snijders, M. Solà, M. Stener, M. Swart, D. Swerhone, V. Tognetti, G. te Velde, P. Vernooijs, L. Versluis, L. Visscher, O. Visser, F. Wang, T. A. Wesolowski, E. M. van Wezenbeek, G. Wiesenekker, S. K. Wolff, T. K. Woo, and A. L. Yakovlev. ADF2019, SCM, Theoretical Chemistry, Vrije Universiteit, Amsterdam, The Netherlands, https://www.scm.com, 2019.

[37] G. t. Te Velde, F. M. Bickelhaupt, E. J. Baerends, C. Fonseca Guerra, S. J. van Gisbergen, J. G. Snijders, and T. Ziegler. Chemistry with adf. *Journal of Computational Chemistry*, 22(9):931–967, 2001.

[38] C. F. Guerra, J. Snijders, G. t. te Velde, and E. J. Baerends. Towards an order-n DFT method. *Theoretical Chemistry Accounts*, 99(6):391–403, 1998.

[39] R. Rüger, A. Yakovlev, P. Philipsen, S. Borini, P. Melix, A. F. Oliveira, M. Franchini, T. van Vuren, T. Soini, M. de Reus, M. Ghorbani Asl, T. Q. Teodoro, D. McCormack, S. Patchkovskii, T. Heine. AMS DFTB 2019.3, SCM, Theoretical Chemistry, Vrije Universiteit, Amsterdam, The Netherlands, https://www.scm.com, 2019.

[40] Band manual 2019. `https://www.scm.com/doc/BAND/index.html`. (Accessed on 11/03/2019).

[41] G. Te Velde and E. Baerends. Precise density-functional method for periodic structures. *Physical Review B*, 44(15):7888, 1991.

[42] SCM. Basis sets and atomic fragments — ADF 2019.3 documentation. `https://www.scm.com/doc/ADF/Input/Basis_sets_and_atomic_fragments.html`. (Accessed on 11/27/2019).

[43] M. Själander, M. Jahre, G. Tufte, and N. Reissmann. EPIC: an energy-efficient, high-performance GPGPU computing research infrastructure, 2019. arXiv: `1912.05848 [cs.DC]`.

[44] A. F. Oliveira, P. Philipsen, and T. Heine. DFTB parameters for the periodic table, part 2: energies and energy gradients from hydrogen to calcium. *Journal of chemical theory and computation*, 11(11):5209–5218, 2015.

[45] S. Grimme, C. Bannwarth, and P. Shushkov. A robust and accurate tight-binding quantum chemical method for structures, vibrational frequencies, and noncovalent interactions of large molecular systems parametrized for all spd-block elements (z= 1–86). *Journal of chemical theory and computation*, 13(5):1989–2009, 2017.

[46] SCM. Geometry optimization, `https://www.scm.com/doc/AMS/Tasks/Geometry_Optimization.html#optimization-methods`. (Accessed on 04/29/2020).

[47] E. Bitzek, P. Koskinen, F. Gähler, M. Moseler, and P. Gumbsch. Structural relaxation made simple. *Physical review letters*, 97(17):170201, 2006.

[48] D. C. Liu and J. Nocedal. On the limited memory BFGS method for large scale optimization. *Mathematical programming*, 45(1-3):503–528, 1989.

[49] K. Hunvik. *Unpublished*.

[50] L. P. Cavalcanti, G. N. Kalantzopoulos, J. Eckert, K. D. Knudsen, and J. O. Fossum. A nano-silicate material with exceptional capacity for CO_2 capture and storage at room temperature. *Scientific reports*, 8(1):11827, 2018.

[51] H. Kalo, W. Milius, and J. Breu. Single crystal structure refinement of one-and two-layer hydrates of sodium fluorohectorite. *Rsc Advances*, 2(22):8452–8459, 2012.

[52] N. Loganathan, G. M. Bowers, A. O. Yazaydin, H. T. Schaef, J. S. Loring, A. G. Kalinichev, and R. J. Kirkpatrick. Clay swelling in dry supercritical carbon dioxide: effects of interlayer cations on the structure, dynamics, and energetics of CO_2 intercalation probed by XRD, NMR, and GCMD simulations. *The Journal of Physical Chemistry C*, 122(8):4391–4402, 2018.

[53] G. M. Bowers, H. T. Schaef, J. S. Loring, D. W. Hoyt, S. D. Burton, E. D. Walter, and R. J. Kirkpatrick. Role of cations in CO_2 adsorption, dynamics, and hydration in smectite clays under in situ supercritical CO_2 conditions. *The Journal of Physical Chemistry C*, 121(1):577–592, 2017.

[54] N. Loganathan, G. M. Bowers, A. O. Yazaydin, A. G. Kalinichev, and R. J. Kirkpatrick. Competitive adsorption of H_2O and CO_2 in 2-dimensional nanoconfinement: GCMD simulations of Cs-and Ca-hectorites. *The Journal of Physical Chemistry C*, 122(41):23460–23469, 2018.

[55] H. T. Schaef, N. Loganathan, G. M. Bowers, R. J. Kirkpatrick, A. O. Yazaydin, S. D. Burton, D. W. Hoyt, K. S. Thanthiriwatte, D. A. Dixon, B. P. McGrail, et al. Tipping point for expansion of layered aluminosilicates in weakly polar solvents: supercritical CO_2. *ACS applied materials & interfaces*, 9(42):36783–36791, 2017.

[56] NiST. CO_2 parameters, `https://webbook.nist.gov/cgi/cbook.cgi?ID=B4000020&Units=SI&Mask=800`. (Accessed on 05/06/2020).

[57] H. D. Young, R. A. Freedman, and R. Bhathal. *University physics: Australian edition*. Pearson Higher Education AU, 2010.

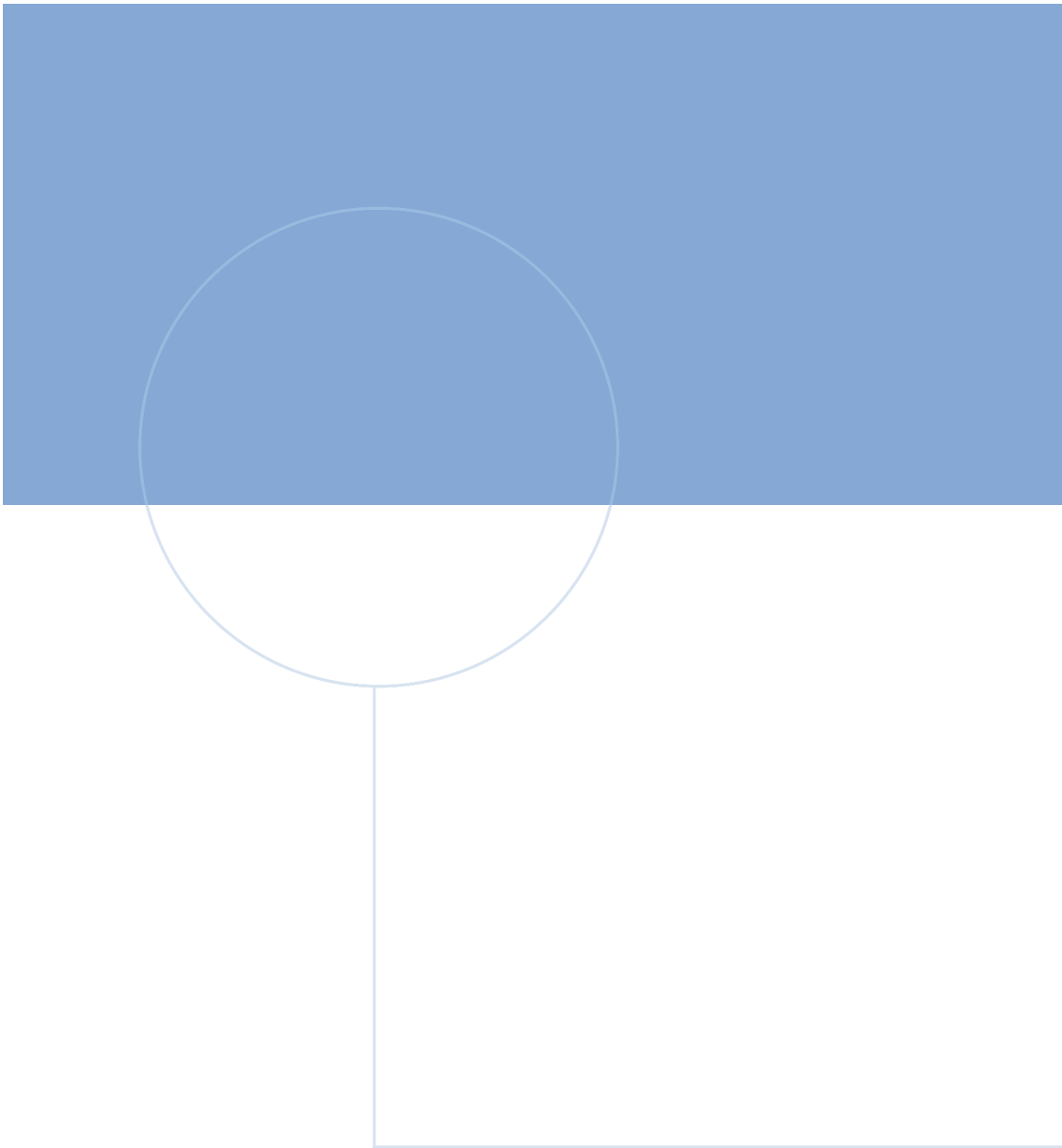

NTNU

Norwegian University of
Science and Technology